INFLUENCE OF NANOPARTICLE SHAPE ON COLLOIDAL PLASMONIC INTERFACE PROPERTIES

A THESIS SUBMITTED TO
THE GRADUATE SCHOOL OF NATURAL AND APPLIED SCIENCES
OF
MIDDLE EAST TECHNICAL UNIVERSITY

BY

ELİF SARIGÜL

IN PARTIAL FULFILLMENT OF THE REQUIREMENTS
FOR
THE DEGREE OF MASTER OF SCIENCE
IN
PHYSICS

SEPTEMBER 2014

Approval of the thesis:

INFLUENCE OF NANOPARTICLE SHAPE ON COLLOIDAL PLASMONIC INTERFACE PROPERTIES

submitted by **ELİF SARIGÜL** in partial fulfillment of the requirements for the degree of **Master of Science in Physics Department, Middle East Technical University** by,

Prof. Dr. Canan Özgen _____
Dean, Graduate School of **Natural and Applied Sciences**

Prof. Dr. Mehmet T. Zeyrek _____
Head of Department, **Physics**

Assist. Prof. Dr. Alpan Bek _____
Supervisor, **Physics Department, METU**

Examining Committee Members:

Prof. Dr. Raşit Turan
Physics Department, METU _____

Assist. Prof. Dr. Alpan Bek
Physics Department, METU _____

Prof. Dr. Mehmet Parlak
Physics Department, METU _____

Assoc. Prof. Dr. H. Emrah Ünalan
Metallurgical and Materials Engineering Department, METU _____

Assoc. Prof. Dr. Mehmet Emre Taşgın
Institute of Nuclear Sciences, Hacettepe University _____

Date: _____

I hereby declare that all information in this document has been obtained and presented in accordance with academic rules and ethical conduct. I also declare that, as required by these rules and conduct, I have fully cited and referenced all material and results that are not original to this work.

Name, Last Name: ELİF SARIGÜL

Signature :

ABSTRACT

INFLUENCE OF NANOPARTICLE SHAPE ON COLLOIDAL PLASMONIC INTERFACE PROPERTIES

Sarıgül, Elif

M.S., Department of Physics

Supervisor : Assist. Prof. Dr. Alpan Bek

September 2014, 66 pages

Nanoparticles bearing free charges, interact very strongly with incoming electromagnetic radiation at certain frequencies called the plasmon resonance frequencies, depending on the size, shape and material properties of the particle and the medium. In order to enhance the light scattering by a two dimensional network of such plasmonic nanoparticles several strategies can be followed. In this thesis, it was pursued the fabrication and characterization of the nanoparticle decorated surfaces by colloidal solution based technique as a self-organized random production method. Optical and spectral electrical properties of plasmonic interfaces were investigated for nanosphere, nanowire and nanobipyramid particles to find out the most efficient geometry. It was also discussed the feasibility of the application of metal nanoparticles to solar cell devices.

Keywords: Metal Nanoparticles, Localized Surface Plasmon Resonance, Colloidal Nanopaticle Solutions

ÖZ

NANOPARÇACIK ŞEKLİNİN KOLOİD PLAZMONİK ARAYÜZ ÖZELLİKLERİ ÜZERİNE ETKİLERİ

Sarıgül, Elif
Yüksek Lisans, Fizik Bölümü
Tez Yöneticisi : Yrd. Doç. Dr. Alpan Bek

Eylül 2014 , 66 sayfa

Serbest yük taşıyan nanoparçacıklar üzerlerine düşen elektromanyetik yayılımla plazmon frekansı adı verilen belli frekanslarda çok güçlü bir şekilde etkileşirler. Bu frekans nanoparçacığın büyüklük ve şekline, içinde bulunduğu ortamın malzeme özelliklerine bağlıdır. Bu plazmonik parçacıklardan oluşan iki boyutlu bir ağın üretilmesinde birkaç farklı strateji takip edilebilir. Bu tezde kendiliğinden oluşma yöntemlerinden biri olan kolloid solüsyonu tekniğiyle nano boyutlarda küre, tel ve bipiramit şekillerinde nanoparçacık dekore edilmiş yüzeyler hazırlanmış ve en uygun geometrinin bulunması amacıyla karakterizasyonlar yapılmıştır. Ayrıca üretilen örneklerin güneş gözesi üzerine uygulanabilirliği tartışılmıştır.

Anahtar Kelimeler: Metal nanoparçacıklar, Yerel yüzey plazmon rezonansı, Koloidal nanoparçacık çözeltisi

Dedicated to my family and the memory of Zeynep Durmuş Çelebi

ACKNOWLEDGMENTS

First of all, I would like to express my tremendous thanks to my supervisor Assist. Prof. Dr. Alpan Bek for his support, guidance and patience along the progress of my study and providing me scientific perspective. I am very grateful to Assoc. Prof. Dr. Yasemin Saraç Oymak, Assoc. Prof. Dr. Hüseyin Oymak for their understanding and being supportive. I am also thankful to Dr. Zaki Saleh and Assoc. Prof. Dr. Emren Nalbant Esentürk for their assistance and contributions.

I am grateful to members of Nano-Optics research group especially to Mona Zolfaghari Borra, Seda Kayra Güllü and Yusuf Kasap for their assistance and to Volkan Hünerli for the SEM session. I am also thankful to members of Atılım University Physics Group for their support. I would like to thank Mete Günöven, Engin Özkol, Zeynep Türkşen Demircioğlu, Şahin Coşkun, Rahim Bahari, Hasan Hüseyin Güllü, Fırat Es, Ertuğrul Karademir, İlkem Evcimen for their precious collaborations throughout this study.

My special thanks go to my family and friends; Zehra Sarıgül, Hüsamettin Sarıgül, Burak Sarıgül, Kerim Sarıgül, Selen Saatci, Emirhan Postacı, Murat Öztürk, Tuğba Okutan and Çidem Argunhan for standing by me and chasing pursuit of happiness together. I am also deeply grateful to Prof. Dr. Betil Başeğmezler, who has been leading intellectual way of thinking since undergraduate years.

The last but not the least, I would like to express my deepest thanks to Burak Duman for his love and encouragement. He has been coworker of the experiments, technical draftsman of the thesis and a ray of sunshine in my life.

TABLE OF CONTENTS

ABSTRACT v

ÖZ vi

ACKNOWLEDGMENTS viii

TABLE OF CONTENTS ix

LIST OF TABLES xi

LIST OF FIGURES xii

LIST OF ABBREVIATIONS xvi

CHAPTERS

1 INTRODUCTION 1

2 THEORETICAL BACKGROUND 7

2.1 Bulk plasmons 7

2.1.1 Drude-Sommerfeld Model 8

2.2 Propagating and Localized Surface Plasmons 9

2.3 Classical Elecrtodynamics and Electrostatic Approximation . 11

2.4 Quasistatic Approximation: Rayleigh Theory 12

2.5 Mie Theory 14

2.6 Tuning the field and scattering enhancement 17

2.7 Thin Film Solar Cell Basics 21

3 EXPERIMENTAL TECHNIQUES 23

3.1 Wet Chemical Process 23

3.2 Colloidal Solution Preparation Procedure 24

3.3 Scanning Electron Microscopy Images 25

3.4 Film Deposition Processes 25

3.5 Optical Characterization 26

3.6 Spectral Photoconductivity Measurement 28

3.7 Image Analysis 29

4 EXPERIMENTAL RESULTS 31

4.1 SEM Images of the Samples 31

4.2 Optical Characterization Results 33

4.2.1 Particle Decorated Sample Characterization 34

4.2.2 Amorphous Silicon Deposited Sample Characterization 37

4.3 Spectral Photocurrent Results 44

5 CONCLUSION 57

REFERENCES 59

APPENDICES

A MIE THEORY 63

LIST OF TABLES

TABLES

Table 3.1 Si_3N_4 and a-Si:H deposition parameters. 26

LIST OF FIGURES

FIGURES

Figure 1.1 Left: Appearance of Lycurgus cup when it reflects the light. Right: Appearance of Lycurgus cup when it transmits the light. 2

Figure 1.2 Gold nanoparticle decoration with e-beam lithography fabrication method, adopted from Tanyeli. 5

Figure 1.3 Monolayer polystyrene sphere formation in the left caption, constituted periodic MNP array in the right caption, adopted from Yu and Zhang. 5

Figure 1.4 Ag NPs formed by dewetting technique on Si_3N_4 layer, adopted from Zolfaghari Borra. 6

Figure 2.1 Schematic view of bulk plasmons. 7

Figure 2.2 Schematic view of propagating surface plasmons. 9

Figure 2.3 Experimental techniques to excite propagating surface plasmon polariton on the metal-dielectric interfaces; (a) Otto configuration, (b) Kretschmann–Raether configuration. 10

Figure 2.4 Schematic drawing of the LSP. 10

Figure 2.5 Mie scattering and Rayleigh scattering. 14

Figure 2.6 Left side: Real part of dielectric function. Right side: Imaginary part of dielectric function of various metals adopted from Benson. 16

Figure 2.7 The fraction of the light scattered into the Si substrate and the relative scattering cross section versus distance graph adopted from Catchpole and Polman. 18

Figure 2.8 Plasmon enhancement versus surface coverage graph of Ag MNPs with varying sizes adopted from Akimov et al. 18

Figure 2.9 The effect of shape and size of the particle on the fraction of light scattered into the substrate adopted from Atwater. 19

Figure 2.10 Usage of plasmonic structures in solar cells: (a) Scattering effect (b) Near-field effect and (c) Back reflector and guiding. 20

Figure 2.11 Schematic energy diagram of valance and conduction bands of semiconductor under (a) zero voltage (b) forward voltage (c) reverse voltage application. 21

Figure 3.1 Appearance of nanowire solution on the left and nanocube solutions on the right with different concentrations. 24

Figure 3.2 Experimental arrangement of reflection and transmission measurements. 27

Figure 3.3 Schematic view of (a) total and (b) diffuse reflection. 27

Figure 3.4 Schematic view of (a) total and (b) diffuse transmission. 28

Figure 3.5 Schematic view of photocurrent measurement for a-Si:H deposited samples without spacer layer. 29

Figure 3.6 Schematic view of photocurrent measurement for a-Si:H deposited samples with spacer layer. 29

Figure 4.1 SEM images of sphere and sphere d. samples. 32

Figure 4.2 SEM images of wire and wire d. samples. 32

Figure 4.3 SEM images of bipyramid and bipyramid d. samples. 33

Figure 4.4 SEM image of bipyramidal particles. 33

Figure 4.5 Total reflectivity, total transmission, diffuse reflectivity, diffuse transmission measurements of (a) sphere sample (b) wire sample (c) bipyramid sample. 35

Figure 4.6 Total reflectivity measurements of (a) sphere and sphere d. samples (b) wire and wire d. samples (c) bipyramid and bipyramid d. samples. . . . 36

Figure 4.7 Haze of (a) sphere and sphere d. samples (b) wire and wire d. samples and (c) bipyramid and bipyramid d. samples. 38

Figure 4.8 Shape dependency of (a) haze and (b) diffuse transmission. 39

Figure 4.9 Shape dependency of (a) total and (b) diffuse reflectivity. 40

Figure 4.10 Extinction of (a) sphere and sphere d. samples (b) wire and wire d. samples (c) bipyramid and bipyramid d. samples. 41

Figure 4.11 Total reflectivity of the (a) sphere samples, (b) wire samples and (c) bipyramid samples after the Si_3N_4 and a-Si:H deposition. 42

Figure 4.12 Total reflectivity of the (a) sphere samples, (b) wire samples and (c) bipyramid samples after the a-Si:H deposition 43

Figure 4.13 Diffuse transmission change for the a-Si:H deposited samples. . . . 44

Figure 4.14 Diffuse transmission graph for nanosphere samples varying with the concentration and presence of spacer layer. 44

Figure 4.15 Shape dependency of differential extinction curve for (a) nanosphere, nanowire and nanobipyramid substrates (b) nanosphere N, nanowire N and nanobipyramid N substrates. 45

Figure 4.16 Haze graphs of a-Si:H deposited samples with the shapes (a) nanosphere (b) nanowire and (c) nanobipyramid. 46

Figure 4.17 Haze graphs of a-Si:H and spacer layer deposited samples with the shapes (a) nanosphere (b) nanowire and (c) nanobipyramid. 47

Figure 4.18 Preferential scattering of the light through the higher refractive index medium when illuminated from (a) glass side (b) a-Si:H side. 48

Figure 4.19 (a) Experimental differential extinction and Mie theory extinction simulation result for a nanosphere deposited with Si_3N_4 and a-Si:H (b) schematic view of calculation of effective dielectric constant. 48

Figure 4.20 (a) Experimental differential extinction and Mie theory extinction simulation result for a nanosphere deposited with a-Si:H (b) schematic view of calculation of effective dielectric constant. 49

Figure 4.21 Extinction and normalized photoresponse graphs of nanosphere substrates with varying concentrations deposited with a-Si:H. 50

Figure 4.22 Extinction and normalized photoresponse graphs of nanowire substrates with varying concentrations deposited with a-Si:H. 51

Figure 4.23 Extinction and normalized photoresponse graphs of nanobipyramid substrates with varying concentrations deposited with a-Si:H. 52

Figure 4.24 Extinction and normalized photoresponse graphs of nanosphere substrates with varying concentrations deposited with Si_3N_4 and a-Si:H. . 53

Figure 4.25 Extinction and normalized photoresponse graphs of nanowire substrates with varying concentrations deposited with Si_3N_4 and a-Si:H. . . . 54

Figure 4.26 Extinction and normalized photoresponse graphs of nanobipyramid substrates with varying concentrations deposited with Si_3N_4 and a-Si:H. 55

Figure 4.27 Absolute values of photocurrent measurements of samples with the spacer layer. 56

LIST OF ABBREVIATIONS

PV	Photovoltaic
NP	Nanoparticle
MNP	Metal nanoparticle
Au	Gold
SP	Surface plasmon
SERS	Surface-enhanced Raman spectroscopy
SEF	Surface-enhanced fluorescence
SOI	Silicon-on-insulator
Ag	Silver
J_{sc}	Short circuit current density
GaAs	Gallium arsenide
SPR	Surface plasmon resonance
e-beam	Electron beam
PSP	Propagating surface plasmon
LSP	Localized surface plasmon
LSPR	Long-range surface plasmon
SPP	Surface plasmon polariton
BEM	Boundary element method
DDA	Discrete dipole approximation
FDTD	Finite difference time domain
MMP	Multiple multipole
FEM	Finite element method
CIGS	Copper indium gallium selenide
Cd-Te	Cadmium telluride
Si_3N_4	Silicon nitrate
a-Si:H	amorphous silicon
PVP	Polyvinylpyrrolidone
NaCl	Sodium chloride

EG	Ethylene glycol
SEM	Scanning Electron Microscope
Au-Pd	Gold-Palladium
PECVD	Plasma enhanced chemical vapor deposition
QTH	Quartz tungsten halogen

CHAPTER 1

INTRODUCTION

In the industrialized developing world, energy consumption increases and there has been more demand on energy resources day by day. According to Renewables 2012 Global Status Report (REN21), only 16.7% of the energy consumption was supplied by renewable energy resources in 2010 [1]. When the energy supplied by the photovoltaic devices and other sources are compared, solar cell market has quite low portion. As the rates of growth of the energy consumption and the solar power coming from the sun ($100\text{mW}/\text{cm}^2$ for AM 1.5 illumination) are concerned, energy produced by photovoltaic (PV) cells should precede. There are various PV device technologies with diverse efficiencies. Although the efficiency of these cells can reach up to 44.7% [2], high cost and high technological requirements limit the production of these cells. Developing technologies show path to produce more effective and low-cost devices. In this sense, thin film solar cell technologies have become a promising way to obtain low cost devices but their efficiencies should be enlarged to be able to compete with other energy resources. Light trapping mechanisms have been used effectively for the enhancement of the devices and plasmonics have become a promising way to increase efficiency of the PV cells while decreasing the cost of the devices. Plasmonic nanoparticles (NPs) can be used in thin film, dye sensitized, crystalline silicon, organic solar cells to increase the efficiency with low cost.

Although the concept of plasmonics has existed for only a century, history of use of metal nanoparticles (MNPs) reaches out ancient times. Accidentally produced Roman glass from 4^{th} century, called Lycurgus cup, has been the first known material that shows plasmonic features. This cup that is shown in the Figure 1.1 looks in different

colors when it reflects and scatters the light due to the presence of gold and silver nanoparticles in its composition. Metal nanoparticles have been used to color the glass in architectural structures as they exhibit extraordinary optical response under light illumination.

Figure 1.1: Left: Appearance of Lycurgus cup when it reflects the light. Right: Appearance of Lycurgus cup when it transmits the light.

Scientific studies of plasmonics have started with Michael Faraday in 1857. He investigated the interaction of light with gold (Au) nanoparticles and compared the properties of MNPs and bulk metal [3]. Then, Maxwell Garnett proposed a model describing optical properties of inhomogeneous bulk dielectric materials that contain metal particles in 1904 [4]. A short time after Garnett, Gustav Mie published solution of Maxwell's equations for homogenous spherical particles in 1908 which is still applied to find scattering properties of the particles.In 1928, the study of Langmuir on classical plasma [5] paved the way to understand quantization of plasma oscillations of valance electrons in solid as a study of Pines and Bohm [6]. Although the study on plasmonics aroused in the end of 19^{th} century, the name of 'plasmon' was first introduced by Pines, as a description of 'quantum of elementary excitation associated with this high-frequency collective motion' in 1956 [7]. Later, the term of surface plasmon (SP) was dubbed by Stern and Ferrell in 1960 [8]. Ritchie's study [9] on plasma losses by fast electrons in thin films was proposal of surface plasmons followed by

the experimental techniques named Otto and Kretschmann configurations of surface plasmon excitation [10, 11]. Later, these theoretical and experimental developments governed the applications of plasmonics on different areas, such as surface enhanced Raman spectroscopy (SERS), surface enhanced fluorescence (SEF), biosensing and photovoltaics.

Stuart and Hall studied on fabrication of 165 nm silicon-on-insulator (SOI) photodetector and found out a factor of 18 enhancement in photocurrent at 800 nm wavelength. This result was obtained for the SOI device assisted with 108 nm mean particle diameter size of silver (Ag) islands overlayer. In addition, photocurrent enhancement was achieved for shorter wavelengths with the same device as well [12]. Schaadt et al. reported enhancement of photocurrent response up to 80% at 500 nm wavelength for Si p-n junction diode decorated with Au colloidal spherical nanoparticles 80 nm in diameter [13]. Pillai et al. investigated the effect of dewetted silver nanoparticles on both wafer based cells and thin SOI devices and achieved sixteen fold and sevenfold enhancement in phortocurrent measurements at 1050 nm for 1.25 μm SOI solar cell device and at 1200 nm for wafer based cell respectively which is also consistent with the modeled results [14]. The research of amorphous silicon p-i-n solar cell carried out by Derkacs et al. exhibited short circuit current density (J_{sc}) increment of 8.3% for the samples assisted with plasmonic enhancement contribution of 100 nm Au particles [15]. Recent study of Axelevitch, Gorenstein and Golan on performance improvement of silicon semiconductor diode has resulted in 10 times increase of open circuit voltage when Au metal nanoparticles are embedded in the p-n junction [16]. Use of plasmonic properties of MNPs is promising way not only for silicon solar cells but also for the organic and other semiconductor solar cells. Morfa et al. studied on bulk heterojunction solar cell decorated with Ag nanoparticle layer and resulted in a factor of 1.7% enhancement in efficiency [17]. Nakayama et al. investigated scattering effect of size- controlled Ag nanoparticles on carrier collection and absorption of gallium arsenide (GaAs) solar cell device and concluded increase in short circuit current density up to 8% [18].

When fluoresecent molecules or atoms are placed nearby the MNPs, fluorescence decay rate can be improved by the help of enhanced field in the vicinity of MNPs. There are a lot of applications, which utilize this property of MNPs such as sur-

face enhanced Raman spectroscopy (SERS), plasmonic antennas, surface enhanced fluorescence (SEF), biological sensing, near-field scanning optical microscopy etc. Quenching or enhancing effects of surface plasmons on the luminescence and Raman scattering signal have been known and they have been used in surface-enhanced fluorescence and surface-enhanced Raman spectroscopy from 1974 till now with the discovery of Fleischmann et al. [19]. Raman signal, which is known to be very weak, can be enhanced up to 12 orders of magnitude by the help of optical nano-antenna effect of plasmonic particles. The non-radiative near-field of the fluorescent molecule is converted into radiating far-field and a factor of 1000 has achieved in fluorescence intensity in the SEF experiments in addition to lowered fluorescence lifetime [20]. These mechanisms have used effectively in bio-sensing applications as well starting from the first use of surface plasmon resonance (SPR) biosensor in 1983 by Liedberg et al. [21].

There are several production methods to form MNPs which comes with both advantages and disadvantages. These fabrication techniques can be examined under three classes; controlled production, self-organized periodic production and self-organized random production.

Electron beam (e-beam) lithography and holographic lithography can be given as an example of controlled production methods. E-beam lithography offers production of wide range of configurations, sizes and shapes of nanoparticles. Particle shapes that are impossible to produce with other methods can be obtained by e-beam lithography[22]. Accuracy in location of the particles can be seen in Figure 1.2 [23]. On the other hand, this fabrication technique requires too much operation time and cost that it can be applied to scales in the order of millimeters. Therefore, e-beam lithography is not applicable for full scale solar cell devices and it can only be used as a proof of concept. Another method, holographic lithography, provides well organized particle distributions as well. However, since it is an optical-based system depending on interference of coherent light sources, it suffers from the diffraction limit which ends up with a drawback to produce particles in nanometer scale.

Nanosphere lithography is a method of self-organized periodic production. Self-assembled, close-packed, monolayer polystyrene spheres are formed on the substrate

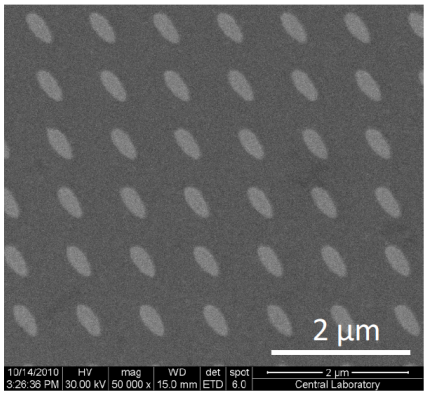

Figure 1.2: Gold nanoparticle decoration with e-beam lithography fabrication method, adopted from Tanyeli.

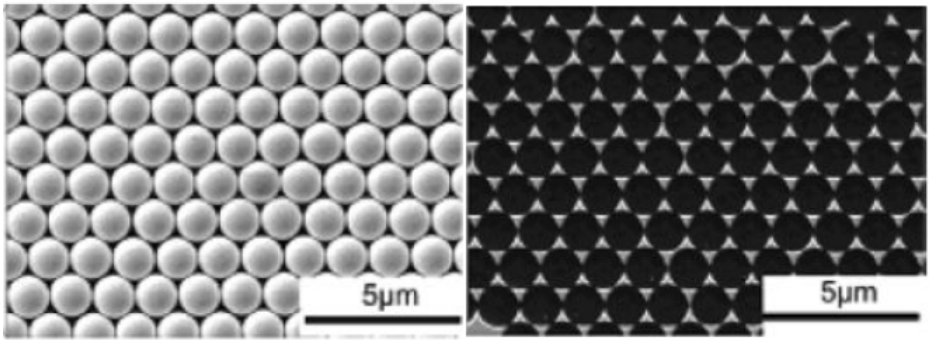

Figure 1.3: Monolayer polystyrene sphere formation in the left caption, constituted periodic MNP array in the right caption, adopted from Yu and Zhang.

as a mask for the easy formation of periodic plasmonic structures. However, perfect control over all the substrate is challenging. Monolayer spheres used as a mask, and acquired periodic structure can be seen in Figure 1.3 [24].

Dewetting technique and colloidal-based production are methods of self-organized random production. Dewetting technique, formation of metal island layer by annealing metal layer, is known to be applicable to large scales as the fabrication method is easy and inexpensive. However, the control on size and shape is not accurate which makes this method disadvantageous. Ag NP assembly produced by dewetting technique is shown in Figure 1.4 [25].

Another self-organized random production method is metal colloid based production and its advantages can be listed as follows. Fabrication of nanoparticle decorated

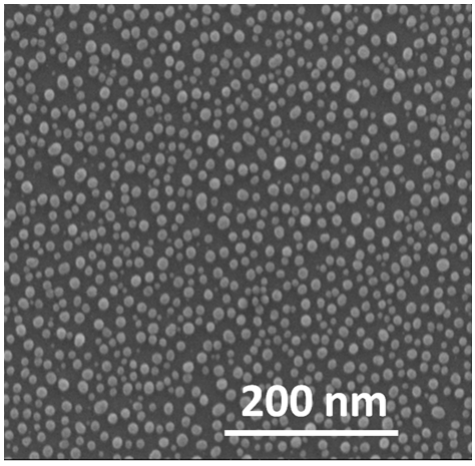

Figure 1.4: Ag NPs formed by dewetting technique on Si_3N_4 layer, adopted from Zolfaghari Borra.

surfaces does not require extended process time. It is applicable to any material with adjustable scales including full scale solar cell devices. Unlike dewetting technique, there is control on the shape and size of the particles. In addition, it is inexpensive to apply, regarding the effort in reduction of production cost. Considering all the benefits, colloid based technique has been chosen to control the size and shape of NPs and this thesis study focuses on the shape effect of the colloidal nanoparticles on plasmonic interfaces.

The thesis consisting of 5 chapters, focuses on the influence of nanoparticle shape on plasmonic properties. In Chapter 1, the study is introduced, state of the art in plasmonics and the fabrication techniques of metal nanoparticles on the substrates are mentioned briefly. In Chpater 2, different approaches of light-particle interaction and theoretical background of plasmons are discussed. All steps of plasmonic interface fabrication and experimental setups used throughout this study are presented in Chapter 3. Experimental results of the study are presented and discussed in Chapter 4. Finally, the thesis study is concluded in Chapter 5.

CHAPTER 2

THEORETICAL BACKGROUND

Noble metals such as Ag, Au, Al etc. are known to conduct heat and electricity due to the existence of free conduction electrons which provides important features that are used in plasmonics. The choice of material for plasmonic applications varies according to the purpose of usage. Although they are different from each other, classical bulk plasma terminology, which was origin of the collective oscillation of electrons in history, can be used to explain the plasmon concept.

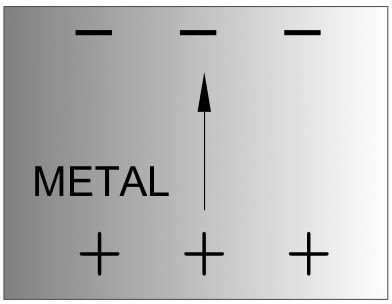

Figure 2.1: Schematic view of bulk plasmons.

2.1 Bulk plasmons

To understand the optical behavior of MNPs, oscillation of free electrons in metal can be considered simply as harmonic oscillation. Plasma oscillation is attributed to Coulomb interaction between charges and motion of free electrons is attributed to damped harmonic oscillation in the presence of positively charged atom core. Drude

model is used to find equation of motion of the free electrons [26]. It is a theory of free electrons in metal that ignores damped oscillation of the free charges which means the theory neglects the bonds between nucleus and electrons. It is practical to find dielectric constant of the materials dependent on the frequency of incoming light. This model gives consistent results in infrared region; however, it is ineffective in the visible range or UV range since there exists contribution from bound electrons too at higher frequencies [27].

2.1.1 Drude-Sommerfeld Model

After Drude model, as a simplest solution case, Lorentz model was introduced with damping term and corrections were made for solid state theory describing optical properties of metal afterwards. Dielectric function found by the theory with additional corrections of Drude model named Drude-Sommerfeld model, is given below. Equation of motion of the electrons under the influence of applied electric field; $\vec{E}(t) = \vec{E_0}e^{-i\omega t}$, is given in the following equation,

$$m_e \left(\frac{\partial^2 \vec{r}}{\partial t^2} + \gamma_d \frac{\partial \vec{r}}{\partial t} \right) = e\vec{E_0}e^{-i\omega t} \tag{2.1}$$

where m_e is the effective mass of free electrons, γ_d is damping term, e is free electron charge and ω is the frequency of the applied electric field. Bulk plasmon frequency; ω_p and dielectric function; $\epsilon_d(\omega)$ are found to be as the following in Gaussian units.

$$\omega_p = \sqrt{\frac{4\pi N e^2}{m_e}} \tag{2.2}$$

$$\epsilon_d(\omega) = \epsilon_\infty - \frac{\omega_p^2}{\omega(\omega + i\gamma_d)} \tag{2.3}$$

N is density of free electrons and ϵ_∞ is ionic background of the metal. Different from bulk plasmons, when there is a metal-dielectric interface, surface plasmons are excited. These surface plasmons can be classified as propagating surface plasmons (PSPs) and localized surface plasmons (LSPs), depending on the structure of the metal that is responsible for the formation of these plasmons that are explained in the next sections. There is also long-range surface plasmon (LRSP) which shows different characteristic since it propagates along the surface up to cm scale.

2.2 Propagating and Localized Surface Plasmons

Surface plasmon polariton (SPP), defined as collective coupling of free charges of the metal and electromagnetic wave on the surface of the conductor, are supported by TM polarized (electric field normal to the metal-dielectric interface) light which can be seen in the Figure 2.2. Electric field which has components in x and z directions excites SPP modes. The generated SP waves at the metal-dielectric interface evanesces into both media in the z-direction; however, penetration depth in dielectric can be 10 times bigger than the metal, which is valuable for the plasmonic applications. This penetration length called skin depth varies in different media since it is inversely proportional to the k-vector (wave vector) in the medium [20].

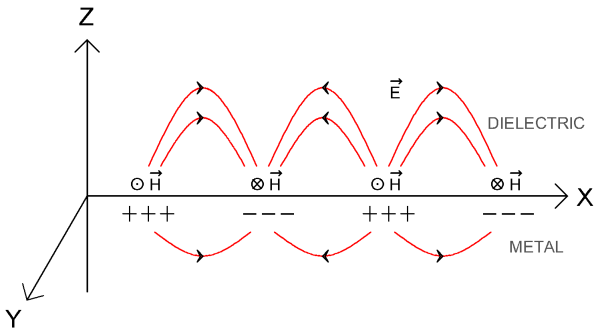

Figure 2.2: Schematic view of propagating surface plasmons.

Two experimental techniques proposed using prism to excite surface plasmons are called Otto and Kretschmann–Raether configurations, which can be seen in Figure 2.3. Surface plasmons are excited by the evanescent field in the air gap between metal layer and prism [10]. Kretschmann–Raether configuration which is slightly different from Otto configuration results in propagating SPP modes at the metal-air interface excited by the evanescent field directly through the metal film [11]. In both configurations, dip in the reflectivity measurement at a certain angle of incidence can be an indicator of generated SPP and enhanced field at the metal-dielectric interface [28].

When the surface plasmons are confined in a metal nanoparticle, LSPs are excited. The size of the particle should be smaller than the wavelength of the light to excite

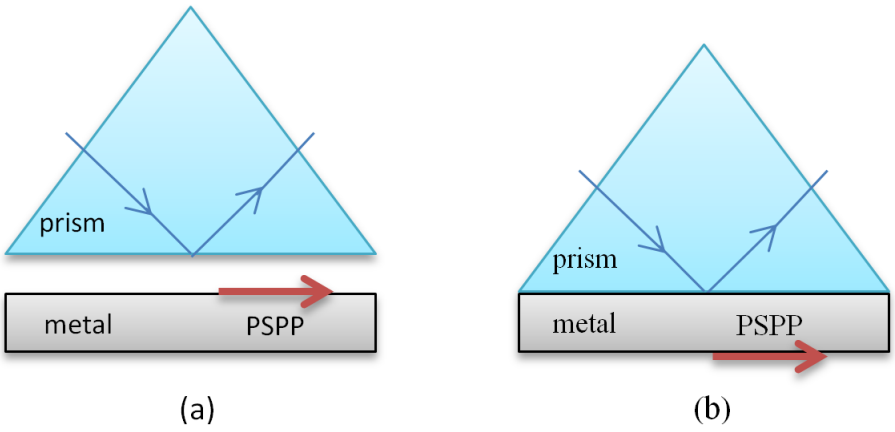

Figure 2.3: Experimental techniques to excite propagating surface plasmon polariton on the metal-dielectric interfaces; (a) Otto configuration, (b) Kretschmann–Raether configuration.

localized plasmons. In the vicinity of the MNPs, very intense electric field is excited at the resonance frequency. Schematic drawing of the LSP can be seen in the Figure 2.4.

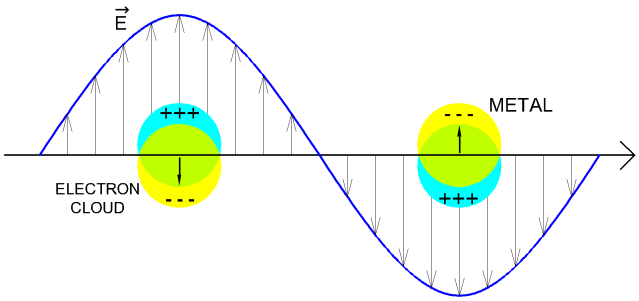

Figure 2.4: Schematic drawing of the LSP.

The energy carried by the electromagnetic wave to be transferred to surface plasmons, the certain conditions should be satisfied. This conditions can be understood by examining theoretical background of SPs starting from Maxwell's equations. There have been several theoretical models proposed describing the interaction of light with MNPs. To solve Maxwell's equations numerical or analytical methods can be used. Analytical solutions of Rayleigh, Mie etc., as early works of plasmonics, led to development of computational methods such as boundary element method (BEM), discrete dipole approximation (DDA), finite difference time domain (FDTD) method, multiple

multipole method (MMP), finite element method (FEM) [29].

2.3 Classical Elecrtodynamics and Electrostatic Approximation

To solve any electrostatic problem one should start from Maxwell's equations which are given in Gaussian units below:

$$\vec{\nabla} \cdot \vec{D} = 4\pi\rho$$

$$\vec{\nabla} \cdot \vec{B} = 0$$

$$\vec{\nabla} \times \vec{H} - \frac{1}{c}\frac{\partial \vec{D}}{\partial t} = \frac{4\pi}{c}\vec{J}$$

$$\vec{\nabla} \times \vec{E} + \frac{1}{c}\frac{\partial \vec{B}}{\partial t} = 0 \tag{2.4}$$

$\vec{E}$ is electric field, $\vec{D}$ is electric displacement, $\vec{B}$ is magnetic induction and $\vec{H}$ is magnetic field. ρ and $\vec{J}$ are defined as electric charge density and current density, respectively. These equations should be solved in problems where there is an interface between two media.

Electrostatic approximation is the solution of electrostatic problem defined by Laplace equation; $\nabla^2\phi = 0$, when there is no electric charge density. The solution is valid in the limit of $\lambda/20$, which implies that the electrostatic solution gives accurate results for the particles smaller than 30 nm in the visible range. Laplace equation can be written as the following in spherical polar coordinates:

$$\frac{1}{r^2}\frac{\partial}{\partial r}\left(r^2\frac{\partial\phi}{\partial r}\right) + \frac{1}{r^2\sin\theta}\frac{\partial}{\partial\theta}\left(\sin\theta\frac{\partial\phi}{\partial\theta}\right) + \frac{1}{r^2\sin^2\theta}\frac{\partial^2\phi}{\partial\varphi^2} = 0 \tag{2.5}$$

The solution of electrostatic potential can be obtained by separation of variables method,

$$\nabla^2\phi(r,\theta,\varphi) = \frac{1}{r}R(r)Y(\theta,\varphi) = 0 \tag{2.6}$$

$$\frac{r^2}{R(r)}\frac{d^2R(r)}{dr^2} + \frac{1}{Y(\theta,\varphi)}\nabla^2_{(\theta,\varphi)}Y(\theta,\varphi) = 0 \tag{2.7}$$

where $\nabla^2_{(\theta,\varphi)}$ is given as

$$\nabla^2_{(\theta,\varphi)} = \frac{1}{\sin\theta}\frac{\partial}{\partial\theta}\left(\sin\theta\frac{\partial}{\partial\theta}\right) + \frac{1}{\sin^2\theta}\frac{\partial^2}{\partial\varphi^2} \tag{2.8}$$

Separable equations are written in terms of separation constant λ;

$$\frac{r^2}{R(r)}\frac{d^2R(r)}{dr^2} = \lambda$$

$$\frac{1}{Y(\theta,\varphi)}\nabla^2_{(\theta,\varphi)}Y(\theta,\varphi) = -\lambda \tag{2.9}$$

These differential equations end up with the most general solution of Laplace equation in spherical polar coordinates where $Y(\theta,\varphi)$ is spherical harmonics.

$$\phi(r,\theta,\varphi) = \sum_{\ell\geq 0}\sum_{m=-\ell}^{\ell}\left(A_{\ell m}r^{\ell} + B_{\ell m}r^{-\ell-1}\right)Y(\theta,\varphi) \tag{2.10}$$

The coefficients $A_{\ell m}$ and $B_{\ell m}$ are determined by applying boundary conditions of the problem. When there is azimuthal symmetry in the problem, i.e for spherical particle, $m = 0$ and solution is reduced into the following form where $P_\ell(\cos\theta)$ is Legendre polynomial.

$$\phi(r,\theta) = \sum_{\ell\geq 0}\left(A_{\ell m}r^{\ell} + B_{\ell m}r^{-\ell-1}\right)P_\ell(\cos\theta) \tag{2.11}$$

Electrostatic potential inside and outside of the sphere in terms of coefficients can be written as the following.

$$\phi_{in} = \sum_{\ell\geq 0} A_{\ell m}r^{\ell}P_\ell(\cos\theta) \tag{2.12}$$

$$\phi_{out} = \sum_{\ell\geq 0}\left(B_{\ell m}r^{\ell} + C_{\ell m}r^{-\ell-1}\right)P_\ell(\cos\theta) \tag{2.13}$$

After finding coefficients from boundary conditions, electric field can be derived from the potential; $\vec{E} = \vec{\nabla}\phi$.

2.4 Quasistatic Approximation: Rayleigh Theory

Elastic scattering of scalar plane wave by particles which are smaller than the wavelength of the incident light was derived by Lord Rayleigh in 1871. Rayleigh approximation is sometimes called dipolar approximation due to the fact that electromagnetic response of the particle is explained by induced dipole and dipolar polarizability of

the particle, which is generally found by electrostatic solution. Scattering cross section is given as [30]

$$\sigma_{sca} = \frac{8}{3}\pi k^4 \left|\alpha\right|^2 \tag{2.14}$$

, where α is polarizability of the particle and k is wave number; $k = \frac{2\pi}{\lambda}$. Under the assumption of isotropic polarizability, absorption cross section is given below.

$$\sigma_{abs} = -4\pi k \mathrm{Im}(\alpha) \tag{2.15}$$

The total extinction cross section can be found by addition of absorption and scattering cross sections;

$$\sigma_{ext} = \sigma_{sca} + \sigma_{abs}$$

Scattering and absorption cross sections explain why absorption dominates for small particles, scattering dominates for bigger particles and the blue color of the sky. Absorption cross section varies proportional to $1/\lambda$ while scattering cross section alters proportional to $1/\lambda^4$, which brings about more scattering in shorter wavelengths. Therefore, size of the particle determines the dominant term in extinction cross section. For the reason that Rayleigh scattering assumes the electric field inside the particle is uniform, this theory is applicable for tiny particles compared to the wavelength of the incoming light. In the end, oscillating dipole results in radiation independent from the direction with the same frequency of incident wave. There is derivation of Lorentz which simplifies the cross sections given above. Under the condition that particles are very small compared to the wavelength and the mean distance between the particles is short in comparison with the wavelength the Lorentz-Lorentz formula relates polarizability with the complex refractive index; $m = n + in'$,

$$4\pi\alpha N = \frac{3\left(m^2 - 1\right)}{m^2 + 2} \tag{2.16}$$

$$\alpha = \frac{3(m^2 - 1)}{4\pi(m^2 + 2)} V = \frac{m^2 - 1}{m^2 + 2} a^3 \tag{2.17}$$

where N is number of particles per unit volume, a is the radius of the sphere. Scattering and absorption efficiency factors become as the following for the spherical particles:

$$Q_{sca} = \frac{8}{3} x^4 \left|\frac{m^2 - 1}{m^2 + 2}\right|^2 \tag{2.18}$$

$$Q_{abs} = -4x\text{Im}\left\{\frac{m^2-1}{m^2+2}\right\} \tag{2.19}$$

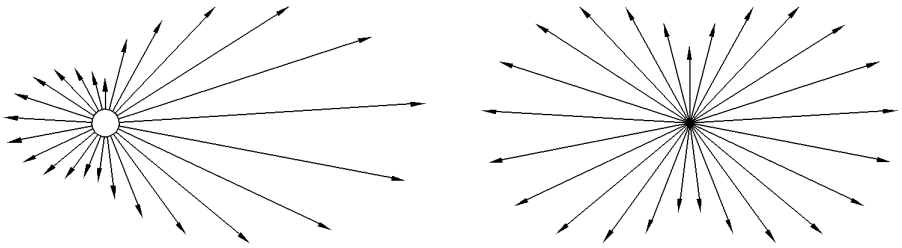

(a) Mie Scattering (b) Rayleigh Scattering

Figure 2.5: Mie scattering and Rayleigh scattering.

The limit for Rayleigh scattering to be accurate Mie parameter which is defined as $x = 2\pi\ a/\lambda$ should be smaller than $0,1$. This result comes from the conditions for Rayleigh scattering which are $x \ll 1$ and $|mx| \ll 1$. More accurate results are obtained by Mie Theory which is valid for all size of the particles. The difference between Mie and Rayleigh scattering was schematized in the Figure 2.5. Theoretical consideration of Mie theory is given in the next section.

2.5 Mie Theory

Mie theory was published by German physicist Gustav Mie in 1908 [31].This theory is a solution method for the elastic scattering of electromagnetic plane wave by an absorbing or non-absorbing spherical particle in a non-absorbing homogenous medium. It is applicable to any size of isotropic homogenous spherical particles. Although Mie theory was derived for the single spherical particle, it can be applied to many particle systems provided that the particles are randomly distributed and the distance between the particles are large compared to the wavelength of the light so that scattered light from each sphere do not interfere with each other. The theory solves Maxwell's equations and derives the wave equation in spherical polar coordinates. When the boundary conditions are applied, the solution is obtained in terms of infinite series expansion of spherical harmonics. Mie theory gives the scattering, extinction, absorption

and backscattering cross sections or efficiencies, angular scattering functions by using only two parameters; relative refractive index of the sphere and ratio of the circumference of the sphere to the wavelength of the electromagnetic wave in the ambient medium. Maxwell's equations bring about the boundary conditions for tangential and normal components as the following:

$$\hat{n} \times (\vec{H_2} - \vec{H_1}) = 0$$

$$\hat{n} \times (\vec{E_2} - \vec{E_1}) = 0$$

$$\hat{n} \cdot ({m_2}^2 \vec{E_2} - {m_1}^2 \vec{E_1}) = 0$$

$$\hat{n} \cdot (\vec{H_2} - \vec{H_1}) = 0 \tag{2.20}$$

In the solution, refractive index of the outside medium is taken as 1 (vacuum) for simplification and refractive index of the particle is denoted as m. Mie Theory ends up with angle dependent cross sections; σ, or efficiency factors; Q. Further information about the derivation can be found in Appendix A. The functions can be integrated over all directions to find total cross sections or efficiency factors. Scattering efficiency factor in integral form is given below as an example;

$$Q_{sca} = \frac{\sigma_{sca}}{\pi a^2} = \frac{1}{x^2} \int_{\pi}^{0} \{i_1(\theta) + i_2(\theta)\} \sin\theta d\theta \tag{2.21}$$

, where i_1 and i_2 are absolute value square of amplitude functions; $i_1 = |S_1(\theta)|^2$ and $i_2 = |S_2(\theta)|^2$. Amplitude functions are used to describe scattering in any direction. Detailed explanations of amplitude function can be found in [30]. This resultant equation is difficult to find numerical results since it is in the form of infinite series. Debye's study on these integral forms of equations resulted in easier relations given below [32]:

$$\sigma_{sca} = \frac{2\pi a^2}{x^2} \sum_{n=1}^{\infty} (2n+1)(|a_n|^2 + |b_n|^2) \tag{2.22}$$

$$\sigma_{ext} = \frac{2\pi a^2}{x^2} \sum_{n=1}^{\infty} (2n+1)\text{Re}(a_n + b_n) \tag{2.23}$$

The terms a_n b_n are the coefficients determined from the solution of Mie. By using the relation between absorption, scattering and extinction; $\sigma_{ext} = \sigma_{sca} + \sigma_{abs}$, absorption cross section can be found in terms of σ_{sca} and σ_{ext}. The first order Mie Theory

results in extinction coefficient, which is defined as $\gamma_{ext}(\omega) = N\sigma_{ext}$ for the medium containing N particles per unit volume is given below:

$$\gamma_{ext}(\omega) = \frac{9N\omega V\epsilon_s^{3/2}}{c}\left(\frac{\epsilon_2(\omega)}{[\epsilon_1(\omega)+2\epsilon_s(\omega)]^2+\epsilon_2^2(\omega)}\right) \tag{2.24}$$

ω is the frequency of incident wave, ϵ_s is dielectric constant of the surrounding medium, V is volume of the particle ϵ_1 and $\epsilon_2$are real and imaginary part of the dielectric constant of the MNP respectively; $\epsilon_m = \epsilon_1 + i\epsilon_2$. This formula explains the resonance condition of the plasmonic particles. For extinction cross section and extinction coefficient to be maximum, denominator should be zero, which is satisfied when $\epsilon_1(\omega) \cong -2\epsilon_s(\omega)$. Strong plasmon resonance occurs at this frequency. This relation between dielectric constants of the particle and surrounding medium shows why metal particle is needed to obtain plasmon resonance. The real and imaginary part of the dielectric function of various metals are given in the Figure 2.6. This figure gives information about the preference of the metal nanoparticle (MNP). Imaginary part of the dielectric function is related to absorption loss of the material. The crucial factors while determining the metal nanoparticle's shape, size and material for application are absorption and scattering efficiencies, the ability to produce plasmon-polariton and the value of the resonance peak wavelength.

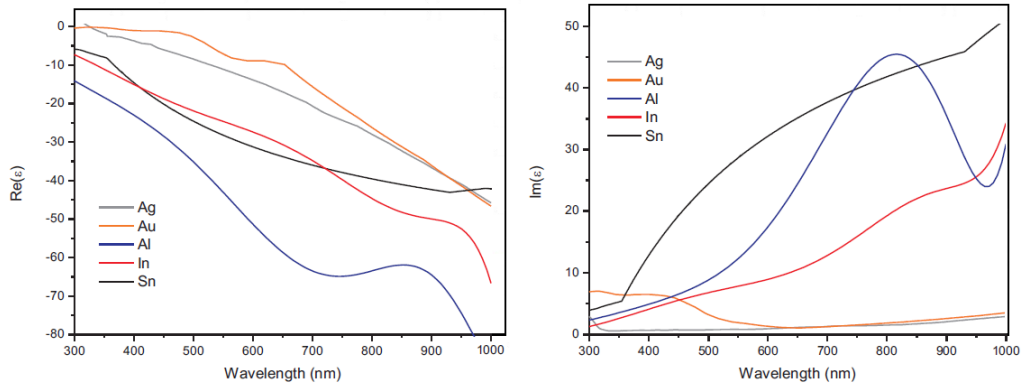

Figure 2.6: Left side: Real part of dielectric function. Right side: Imaginary part of dielectric function of various metals adopted from Benson.

There are softwares which give scattering or extinction cross sections by applying Mie Theory in literature. In this study, one of the softwares have been used with assigned effective refractive index of the surrounding medium of the MNP to compare

Mie theory and experimental results for the spherical particles [33]. Details of the simulation are presented in Chapter 4.

2.6 Tuning the field and scattering enhancement

Nowadays, recent technologies make way for tuning resonance wavelength precisely. Field enhancement can be tuned by changing the fraction of the light guided into the active layer of the solar cell. In that sense, to increase the scattering cross section, the size of the MNP can be enlarged up to a critical point at which scattering cross section starts to decline. At the plasmon resonance, it is known that the scattering cross section can be 10 times of the geometrical cross section of the nanoparticle. Existance of spacer layer can change the scattering cross section and the fraction of the light scattered into the substrate abruptly, which can be seen in Figure 2.7 [34]. Theoretical studies show that resonance frequency of dipole mode and quadrupole modes should be tuned about 400 nm and 700 nm, respectively, to obtain the optimum enhanced absorption [35]. At this point, there is a mechanism that should be mentioned called up-conversion. Enhancement in extinction is achieved by the excitation of higher order plasmon modes of the MNPs. Therefore MNPs can be used as upconverting materials to produce photons with higher energies by using lower energy photons. Thus, MNPs are used to make contribution to the photovoltaic efficiency from the near infrared region of the solar spectrum. On the other hand, the usage of the MNPs may cause reflection increase in shorter wavelengths. Therefore, structures decorated with MNPs should be designed considering this dilemma. This can be achieved by changing parameters such as size, shape of the MNP or the refractive index of the passivation layer around MNPs.

Plasmon oscillation, which contributes to increase in scattering and absorption cross section, decays in time and it can be via radiative decay or interband transitions. When interband transition occurs, plasmon oscillations decay into electron hole pairs [36].

Cathpole and Polman studied on the effect of particle shape and the material on the path length enhancement resulted in that fraction of light scattered into the semi-

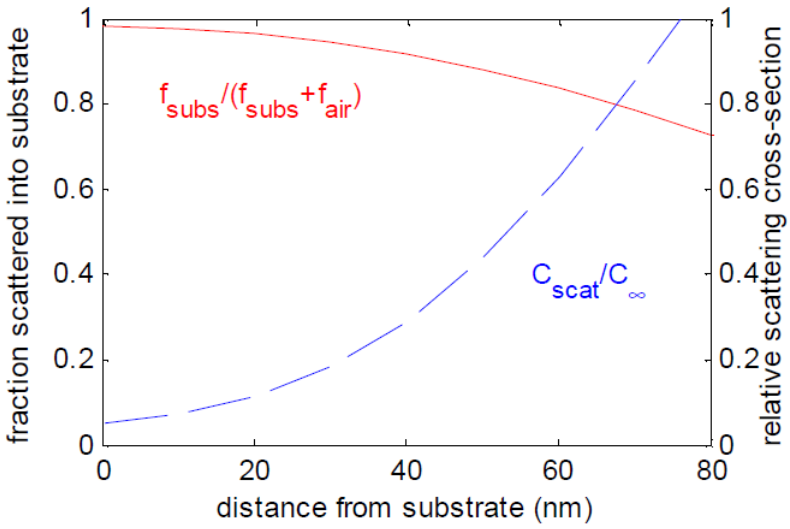

Figure 2.7: The fraction of the light scattered into the Si substrate and the relative scattering cross section versus distance graph adopted from Catchpole and Polman.

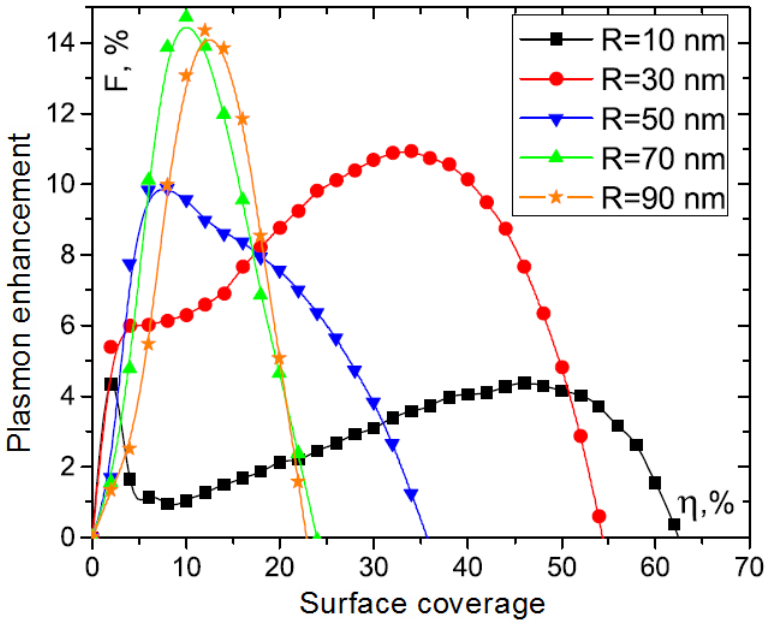

Figure 2.8: Plasmon enhancement versus surface coverage graph of Ag MNPs with varying sizes adopted from Akimov et al.

conductor changes with both shape and size of the particle. Simulation with FDTD method showed that cylindrical or hemispherical particles which have larger contact area between the particles and substrate scatter the light into the substrate more than spherical particles as a consequence of decline in evanescent wave through the

air. Comparison of size of the spheres indicates that bigger particles should be preferred to obtain more scattering into the semiconductor [37]. The change of fraction scattered into the substrate for various shapes can be seen in Figure 2.9 [38]. The calculations of plasmon enhancement with varying particle diameters show that around 10% coverage results in the best efficiency for the particle radius about 70 nm, which can be seen in Figure 2.8 [35].

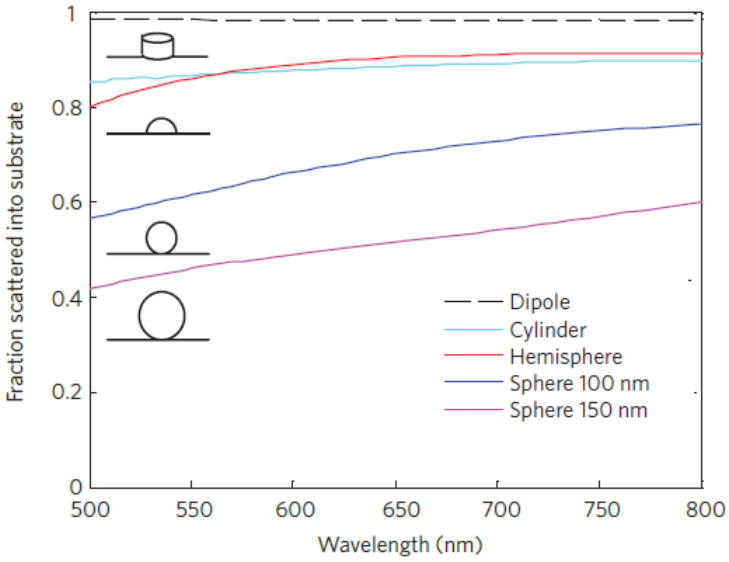

Figure 2.9: The effect of shape and size of the particle on the fraction of light scattered into the substrate adopted from Atwater.

Theoretical enhancement limit differs with the size of the particles. For small particles, (about 30 nm) absorption dominates and maximum enhancement is around 11% , while around 15% enhancement can be achieved for bigger particles (about 80 nm) [35]. Ag particles yielded 17 times path length enhancement for the Si substrates with 10 nm thick Si_3N_4 spacer layer. The same simulation repeated with Au particles resulted in 8 times path length enhancement, which shows that Ag particles give better scattering efficiency than the Au particles due to being less absorbing. Imaginary part of the dielectric function is related to the absorption of the material and it can be seen for several metals in Figure 2.6.

An enhancement in photocurrent can be obtained by using MNPs and this improvement can be explained by different mechanisms. Plasmonic structures in PV devices

and their effects can be classified into three mechanisms, which can be seen in Figure 2.10.

In the first mechanism, NPs increase the light scattering and absorption due to the existence of localized surface plasmons (LSP) in the vicinity of MNPs. This phenomenon can be considered as far field effect. MNPs are used to improve the preferential light scattering into the substrate by placing them on the top of the active layer. To increase forward scattering into dielectric medium, bigger MNPs around 100 nm should be preferred. These structures also contribute to light trapping in the dielectric medium.

Second mechanism is to get benefit from the enhanced electric field generated around the MNPs by embedding the particles into the substrate. In this configuration, excited field around the particles can contribute the production of electron hole pairs in the semiconductor. Near field effect occurs at the vicinity of metal particles that leads to electromagnetic field enhancement up to several orders of magnitude in that region. This antenna effect occurs for the small particles which have less absorption coefficients.

Last method is to use MNPs as back reflector of the solar cells for wave guiding. Surface plasmon polaritons can propagate through the metal-dielectric interface. Instead of using grating, use of MNPs can be an alternative way of light trapping mechanisms.

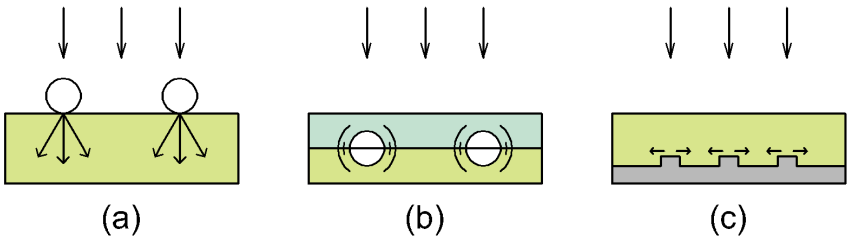

Figure 2.10: Usage of plasmonic structures in solar cells: (a) Scattering effect (b) Near-field effect and (c) Back reflector and guiding.

2.7 Thin Film Solar Cell Basics

Thin film solar cells are second generation photovoltaic devices such as copper indium gallium selenide (CIGS) solar cells, cadmium telluride (Cd-Te) solar cells, dye-sensitized solar cells or amorphous silicon solar cells. The main purpose of thin film solar cell production is to reduce raw material cost. However, while decreasing the cost of the PV devices, the efficiency of the cell reduces as well compared to single or multicrystalline silicon solar cells. This obstacle brings about use of different mechanisms to increase the efficiency, such as surface texturing and plasmonic applications.

The materials used as active medium for photovoltaic devices should absorb the incoming light effectively. Various light trapping mechanisms are applied to semiconductors having low absorption coefficient. For example; the surface of thick silicon solar cells composed of crystalline silicon is textured to obtained pyramidal structures on the substrate. These structures are used effectively to increase the absorption and path length of the light within the active region. Considering the thickness of the thin film solar cells, texturing is not an applicable process. Plasmonic NP can be used to solve this problem.Plasmonic NPs are not only applicable to thin film solar cells; but also to the wafer based solar cells.

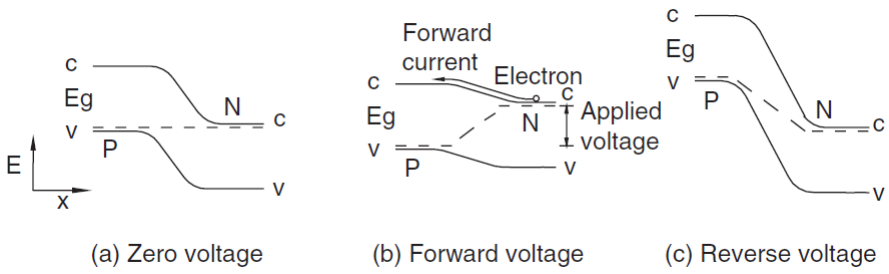

Figure 2.11: Schematic energy diagram of valance and conduction bands of semiconductor under (a) zero voltage (b) forward voltage (c) reverse voltage application.

The main working principle of solar cell is based on generating electron hole pairs by absorbing incoming light. When the incoming photon energy is equal or greater than the bandgap of the semiconductor used in solar cell, this photon is absorbed by the electron which goes to conduction band from valance band. This leads to hole generation in the valance band. To collect electrons and holes before they recombine, PV cell composes of p and n type of semiconductors and contacts on them, which

collect the generated holes and electrons respectively . In Figure 2.11 it can be seen that the built in electric field that forces the separation of electron hole pairs in the p-n junction potential.

CHAPTER 3

EXPERIMENTAL TECHNIQUES

In this chapter, experimental details of the thesis study are presented.

3.1 Wet Chemical Process

Ag and Au MNPs were deposited onto glass substrates by spin coating method. Before the decoration with MNPs, glass substrates were cut into pieces with sizes 1.0x1.0 cm^2 and 2.5x2.5 cm^2 for SEM imaging and optical measurement processes respectively. Glass substrates were subjected to cleaning process before the MNP decoration. Glasses were cleaned subsequently with deionized water, acetone and isopropyl alcohol in an ultrasonic cleaning bath for at least ten minutes. Then, they were placed in piranha solution for fifteen minutes which is obtained by addition of hydrogen peroxide (H_2O_2) to sulfuric acid (H_2SO_4) with a ratio 1:3. After the removal of piranha solution, the samples were dried by using a nitrogen gun. All samples, produced by wet chemical process, were prepared in GÜNAM Clean Room at room temperature. Before the nanoparticle decoration, the colloidal solutions were homogenized by using ultrasonic bath and vortex. To decorate the substrates, samples were placed to spin-coater and prepared solution was added dropwise. The samples were kept waiting for 7.5 minutes before the spinning process. They were spincoated with 2000 rpm for 45 seconds.

Colloidal solutions containing Ag nanospheres, nanowires, and bipyramids were synthesized at the Department of Metallurgical and Materials Engineering of Middle East Technical University in Nanomaterials and Devices Laboratory. Appearance of

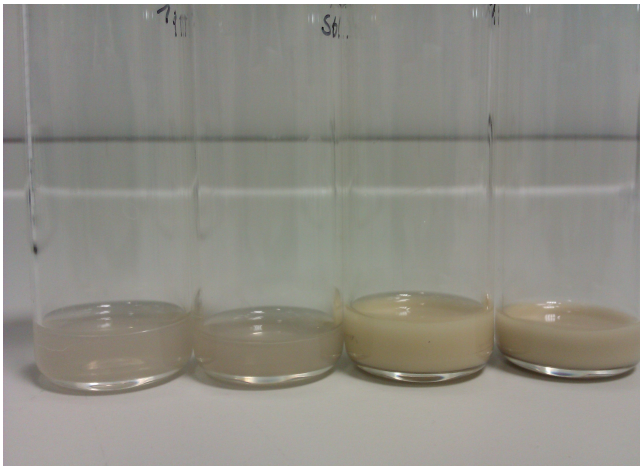

Figure 3.1: Appearance of nanowire solution on the left and nanocube solutions on the right with different concentrations.

nanowire and nanocube solutions can be seen in Figure 3.1 with different concentrations. Each colloidal solution was diluted to observe the concentration effect besides the effect of shape. Each solution with different shape of NPs was applied to the glass substrates with two concentrations. Two sample sets were prepared. One set was deposited with silicon nitrate (Si_3N_4) and amorphous silicon (a-Si:H), and the other set was deposited with a-Si:H only. Deposition processes of Si_3N_4 and a-Si:H are given in the following section.

3.2 Colloidal Solution Preparation Procedure

Ag nanowires were synthesized by self-seeding polyol process. In this technique, an inorganic salt is reduced by a polyol and agglomeration of particles is prevented by addition of surfactant, which is commonly polyvinylpyrrolidone (PVP). Required chemicals were bought from Sigma-Aldrich company. 7 mg of sodium chloride (NaCl) was added into 10 mL of 0.45 M ethylene glycol (EG) solution of PVP and heated at 170°C. By using injection pump, solution of 0.12 M $AgNO_3$ in 5 mL of EG added dropwise at a rate of 5 mL/h. During this process, solution was stirred (1000 rpm) by a magnetic stirrer. After the drop-wise EG addition process, solution was heated up at 170°C for 30 minutes and was cooled to room temperature. To enable the removal of polymer from the solution, the diluted solution with acetone was cen-

trifuged two times for 20 minutes at 6000 rpm. Then, nanowires were dispersed in ethanol and centrifuged again under the same conditions. In the end of this procedure, nanowires with 60 nm diameter and length of 8 to 10 microns were obtained. The solution was subjected to ultrasonic vibration to decrease the length of the wires to around 1 micrometer.

Synthesis of Ag nanospheres carried out with a modified procedure of wire synthesis without the addition of NaCl and Ag nanospheres of around 100 nm diameter were obtained [39].

Solution containing bipyramids of Ag was synthesized with polymer-mediated polyol process as well. 94 mM $AgNO_3$ was added to 3 mL EG solution. Another 3 mL of EG solution containing 0.11 mM NaBr and 144 mM PVP was prepared and two solutions added dropwise into heated EG solution of 5 mL in an oil bath at 160°C in which contains 30 μL of 10 mM NaBr. 5 hours later, bipyramids solution was obtained [39, 40].

3.3 Scanning Electron Microscopy Images

Scanning electron Microscopy (SEM) images of the samples were taken by QUANTA 400F Field Emission SEM device with 1.2 nm resolution in the Central Laboratory at METU to observe the morphology of the samples. 1x1 cm^2 glass substrates were coated with gold-palladium (Au-Pd) layer about 15 nm with Polaron Range sputter coater before imaging to provide the conductivity of the samples.

3.4 Film Deposition Processes

After the NP decoration, a 20 nm thin layer of Si_3N_4 and 220 nm layer of hydrogeneted amorphous silicon (a-Si:H) were deposited on the substrates by using plasma enhanced chemical vapor deposition (PECVD) system at GÜNAM. Si_3N_4 coating was considered to be a buffer layer to prevent current flow directly through the nanoparticles while conducting the PC measurements and also serve for surface passivation. Si_3N_4 and a-Si:H deposition reactions via PECVD are given below, re-

Table 3.1: Si_3N_4 and a-Si:H deposition parameters.

Deposition parameters	Si_3N_4	a-Si:H
Temperature:	200°C	200°C
Pressure:	1 Torr	1 Torr
RF Power:	100 W	50 W
SiH_4 flow rate:	250 Sccm	350 Sccm
NH_3 flow rate:	50 Sccm	-
Deposition duration:	30 sec	8 min
Thickness of the coating:	20 nm	220 nm

spectively:

$$SiH_4(gas) \longrightarrow Si(solid) + 2H_2(gas)$$

Si_3N_4 deposition process in PECVD is given below:

$$3SiH_4(gas) + 4NH_3(gas) \longrightarrow Si_3N_4(solid) + 24H_2(gas)$$

Table 3.1 shows Si_3N_4 and a-Si:H deposition parameters.

3.5 Optical Characterization

Diffuse and specular spectrophotometric measurements for reflectance and transmittance were carried out in the Optical Characterization Laboratory at the department. Optical characterization was made within the 400-1100 nm wavelength range for the glass samples decorated with nanoparticles and the same samples after the Si_3N_4 and a-Si:H depositions. To see the effect of nanoparticles and coatings, the same measurements were carried out for the samples without the nanoparticle decoration. These samples are referred as reference samples. Schematics of the optical characterization setup is given in Figure 3.2.

250 W quartz tungsten halogen (QTH) Lamp was used and the spot size of the light was arranged with a ACL4532 aspheric lens and aperture. Light beam was chopped with chopper wheel connected to a controller. The chopped light beam was collimated through the transmission port of the 8 inch integrating sphere (Oriel, Model number 70679NS) and spectral analysis was carried out by monochromator (Oriel,

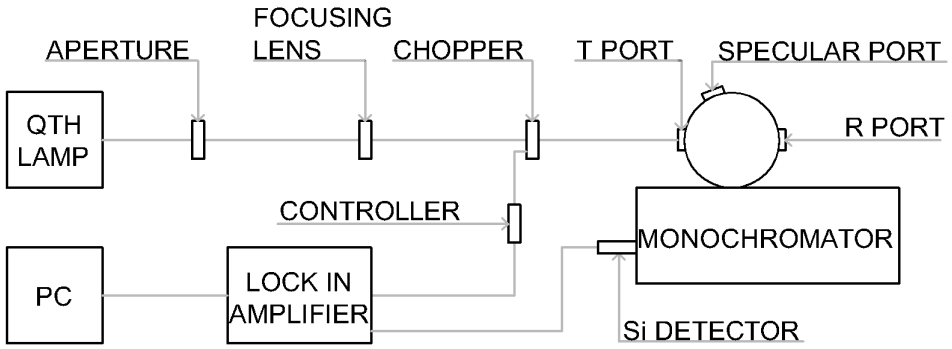

Figure 3.2: Experimental arrangement of reflection and transmission measurements.

Model number 74100) connected to a UV enhanced Si detector (Oriel, Model number 70356), lock-in amplifier and computer with installed GPIB interface and Labview software.

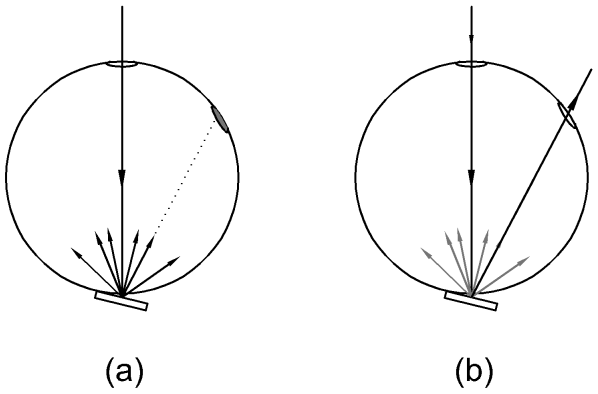

Figure 3.3: Schematic view of (a) total and (b) diffuse reflection.

Before the measurement of samples, background measurement was taken and calibration was done with $BaSO_4$ reference disk, which has 100% reflectance. The size of the samples were arranged to be at least 2.5x2.5 cm^2 to be fit into the ports. For the total transmittance measurement, sample was placed at the transmission (T) port where the reflection (R) port is covered with $BaSO_4$ calibration disk. To obtain the diffuse transmittance, measurement was repeated with open R port. For the reflectance measurement, sample was mounted in the R port and specular R port was closed

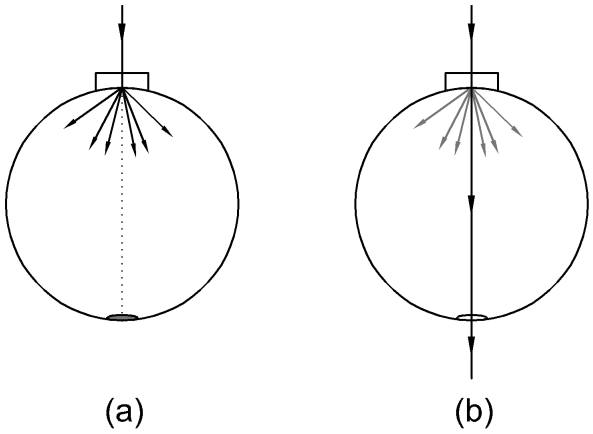

Figure 3.4: Schematic view of (a) total and (b) diffuse transmission.

and opened with the $BaSO_4$ disk for the total and diffuse reflectance measurements, respectively. The samples placed in the R port of the integrating sphere were illuminated by the incident light with tilted angle of 4° from the normal direction. This tilted configuration provided opportunity to measure diffuse reflectance by opening the specular port to let the specular reflected light get away from the port. Figure 3.3 shows the difference between total reflectivity, diffuse reflectivity and the difference between total transmission and diffuse transmission is shown in the Figure 3.4.

3.6 Spectral Photoconductivity Measurement

After the reflection and transmission measurements, parallel aluminum contacts were deposited on the same samples by thermal evaporation method. Parallel contacts were made by using shadow mask made of silicon with length a of 1 cm, width of 2 mm and gap of 1 mm between contacts. Then, samples were annealed for 1 hour in an oven under nitrogen flow. Photoresponse of the samples were determined by current measurement under bias voltage varying from -10 V to +10 V. This measurement was carried out in dark and under the illumination of QTH lamp. Figure 3.5 and Figure 3.6 show the schematic drawing of the cross sections of samples prepared for the photocurrent measurements. The Figure 3.5 shows the samples without the spacer layer deposition and Figure 3.6 shows the samples with spacer layer deposition. Spectral

photocurrent was measured at 10 V in the range of 400 to 1100 nm. Photocurrent data was divided into the incident power coming out of the monochromator for normalization.

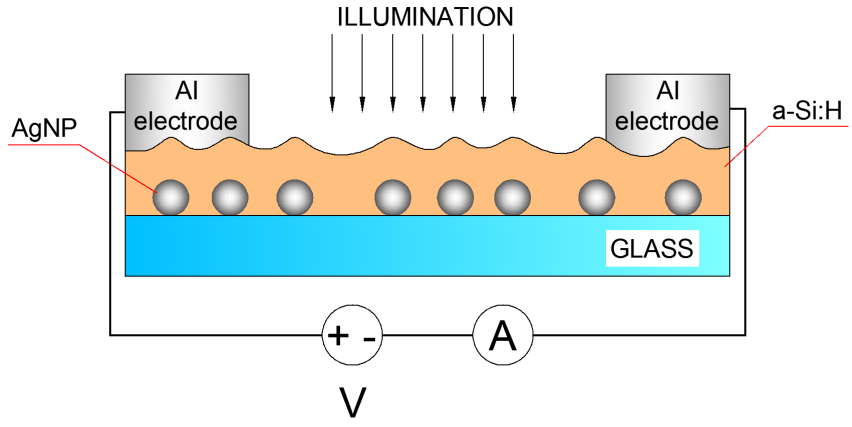

Figure 3.5: Schematic view of photocurrent measurement for a-Si:H deposited samples without spacer layer.

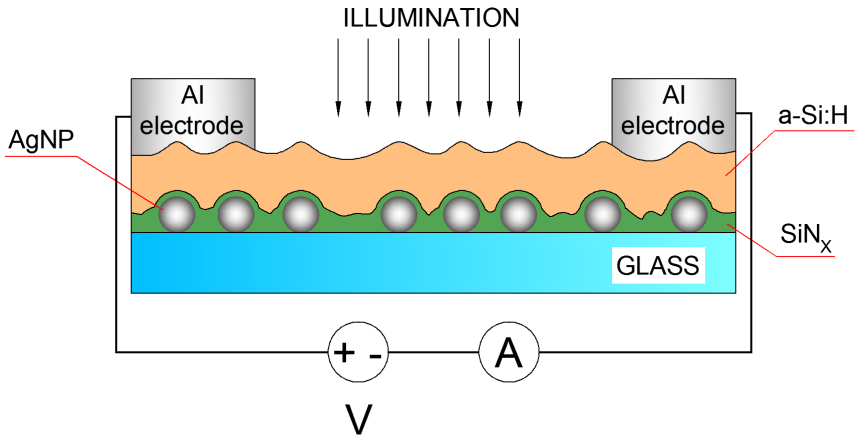

Figure 3.6: Schematic view of photocurrent measurement for a-Si:H deposited samples with spacer layer.

3.7 Image Analysis

SEM images of the samples were analyzed to find out the surface coverage of the Ag MNPs. Image analysis was carried out with a software called Gwyddion. MNPs were marked with grains by using contrast between MNPs and the surface of the substrate.

The SEM images of samples with varying magnifications were averaged for better surface coverage estimation.

CHAPTER 4

EXPERIMENTAL RESULTS

In this chapter, experimental results of the thesis study are presented. In this study, three different colloidal solutions were used namely Ag nanospheres, Ag nanowires and Ag nanobipyramids. The purpose was to see the effect of the surface coverage beside the effect of the nanoparticle shape. For that reason, each nanoparticle colloidal solution was used in two different concentrations. Colloidal solutions which were prepared according to the recipe written in the Colloidal Solution Preparation Procedure section were used directly for the samples denoted as sphere, wire and bipyramid. Each solution was diluted in the entrainment ratio of 1:1 with the solvent of the solution. The samples prepared with the diluted solutions were denoted as sphere diluted (sphere d.), wire diluted (wire d.) and bipyramid diluted (bipyramid d.) later on. Two sets of samples were prepared to deposit a-Si:H for the photoconductivity measurements. One of these sets was deposited with a thin layer of silicon nitrade before the a-Si:H deposition to see the effect of the passivation. These samples were denoted as sphere N, sphere d. N, wire N, wire d. N, bipyramid N and bipyramid d. N later on.

4.1 SEM Images of the Samples

SEM images of nanosphere, nanowire and nanobipyramid solutions with two different concentrations are shown in the Figure 4.1, Figure 4.2 and Figure 4.3, respectively. SEM image of bipyramids at a higher magnification can be seen in the Figure 4.4 clearly. It can be seen in the SEM images that the uniformity has mostly achieved in

bipyramid samples where there exists local agglomerations in all samples; especially in nanowire samples.

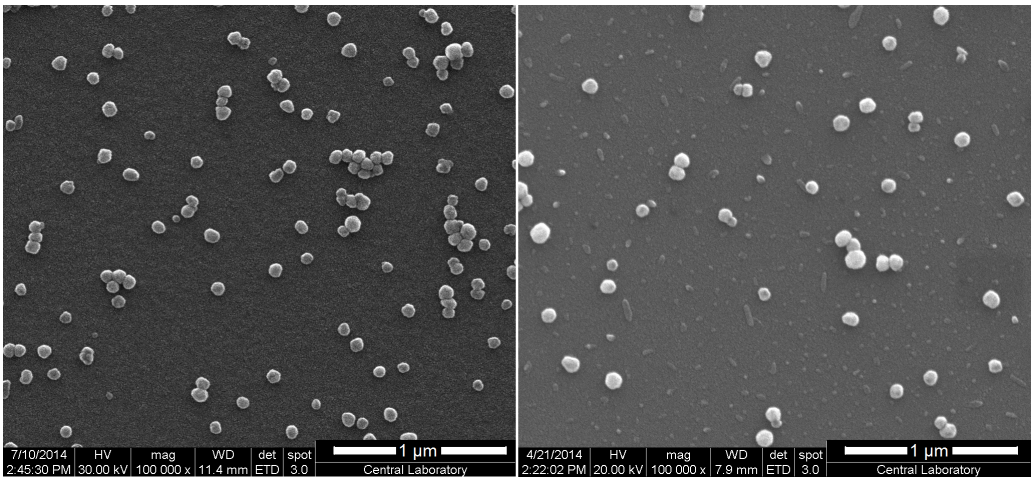

Figure 4.1: SEM images of sphere and sphere d. samples.

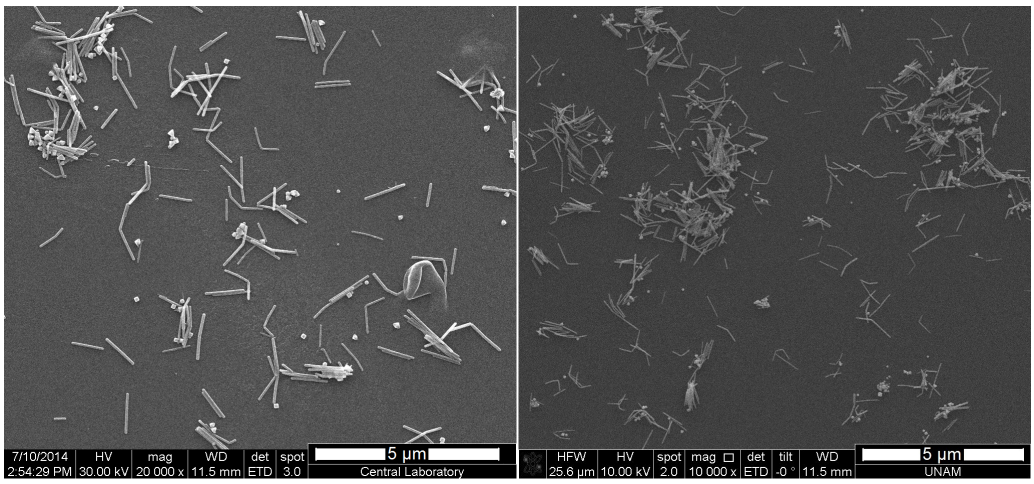

Figure 4.2: SEM images of wire and wire d. samples.

Samples decorated with nanosphere solution and diluted nanosphere solution resulted in surface coverages of 7% and 5%, respectively. NanoWire and diluted nanowire solution substrates revealed surface coverages of 10% and 8%, respectively. 20% and 8% surface coverages were obtained with the nanobipyramid and diluted nanobipyramid solutions, respectively.

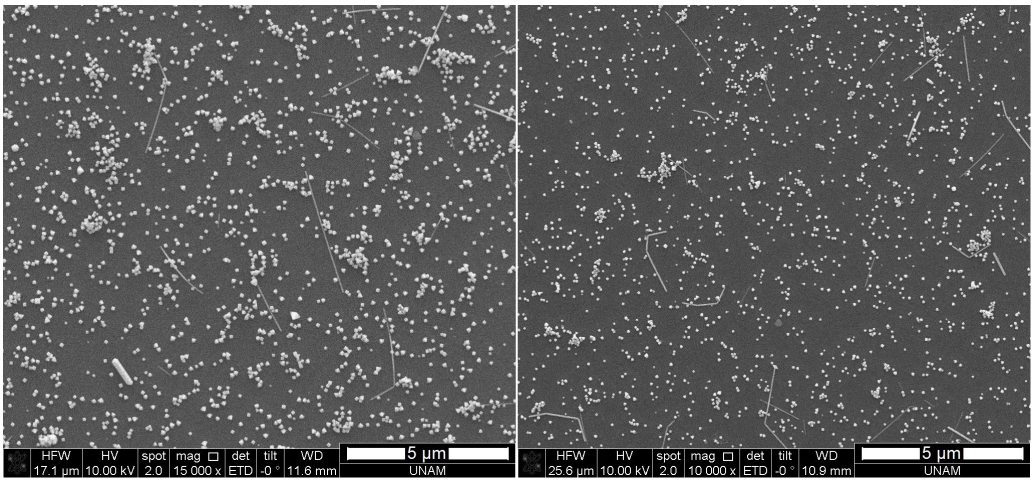

Figure 4.3: SEM images of bipyramid and bipyramid d. samples.

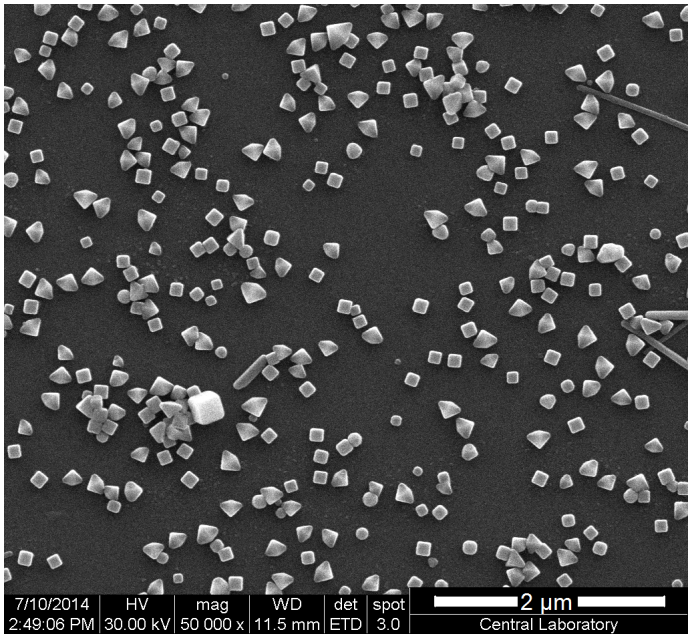

Figure 4.4: SEM image of bipyramidal particles.

4.2 Optical Characterization Results

Optical characterization of the samples was carried out after the MNP decoration and a-Si:H deposition. The results are presented in the next subsections.

4.2.1 Particle Decorated Sample Characterization

All measurements were carried out for each side of the samples: Light shone from the particle side and the glass side of the substrates were denoted as front and back, respectively. In Figure 4.5 total reflectivity, total transmission, diffuse reflectivity and diffuse transmission measurements are shown. Since glass substrates were decorated with the MNPs, they possessed low reflectivity and high transmission.

In Figure 4.6, total reflectivity results of all samples from particle and glass side are shown. Total reflectivity measurements resulted in higher reflectivity when the samples were illuminated from the glass side of the samples except for the bipyramid samples. Sphere samples gave the least total reflectivity and samples decorated with bipyramids resulted in the most total reflectivity as expected since the surface coverage of the sphere samples were too small compared to the bipyramid samples.

Haze of the samples, which is defined as the ratio of diffuse transmission to total transmision was plotted in the Figure 4.7. It is desired for the MNPs to scatter the light in the longitudinal direction to be able to get benefit from the plasmonic effects in the junction of the solar cells. Therefore, the number of charge carriers excited in the junction can be enlarged. MNPs are also used to increase path length of the light in the semiconductor by increasing diffuse scattering into the substrate. Whether there is any increment in path length or diffuse scattering can be inferred from the haze measurement. It can be seen that samples with surface coverage about 10% led to a 3 to 5 times increase in haze. MPSs raised the scattering in longitudinal direction. Haze and diffuse transmission showed the same spectral characteristics depending on the shape of the MNPs, which can be seen in Figure 4.8. In the Figure 4.8, it was compared how the haze and diffuse transmission changed with the shape of the MNPs. To see the effect of the shape, samples with the same concentration but different shapes were chosen in these plots. Enhancement occurred in haze and diffuse transmission independent from the wavelength for the nanowire and nanosphere samples. On the other hand, it was observed that haze and diffuse transmission gave a peak around 520 nm for the nanobipyramid samples. 9 and 4 fold enhancements in haze were observed for the nanowire and nanosphere particles, respectively. The diffuse transmission exhibited a 300% and 700% increase for the nanosphere and

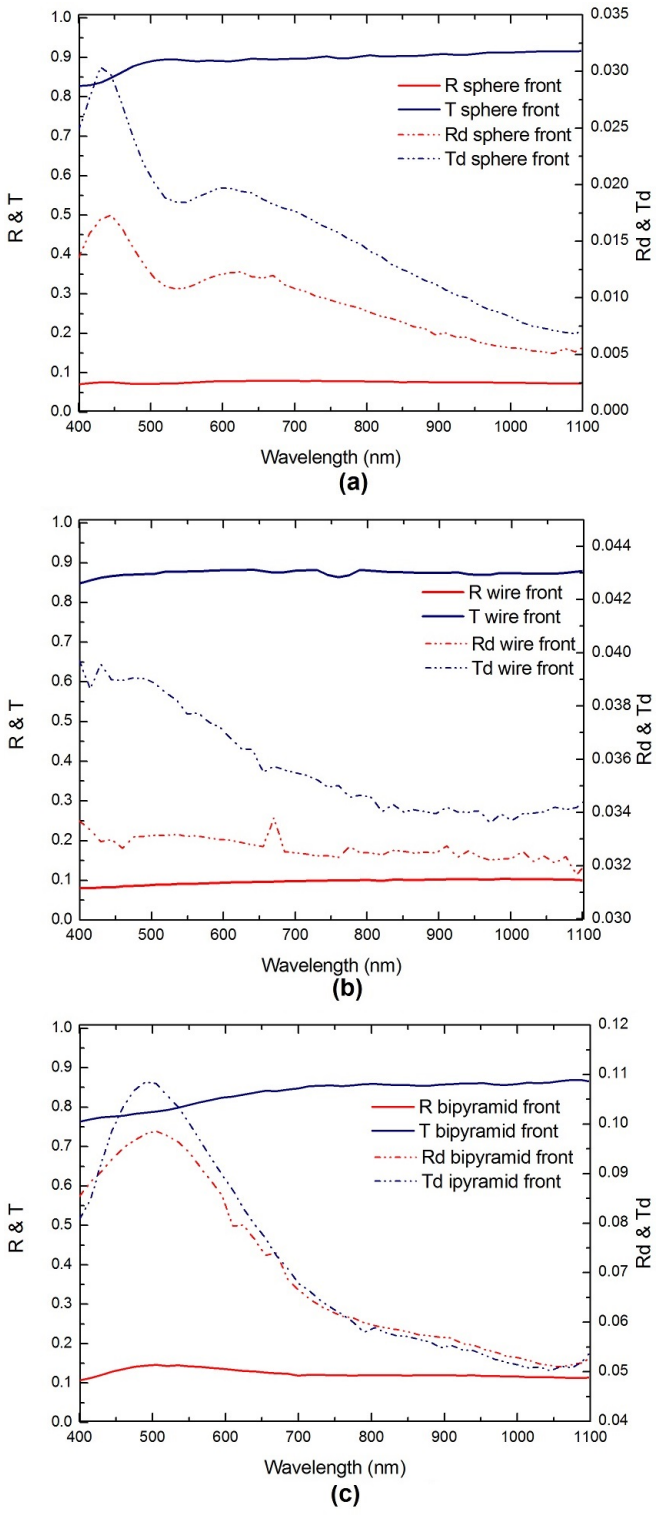

Figure 4.5: Total reflectivity, total transmission, diffuse reflectivity, diffuse transmission measurements of (a) sphere sample (b) wire sample (c) bipyramid sample.

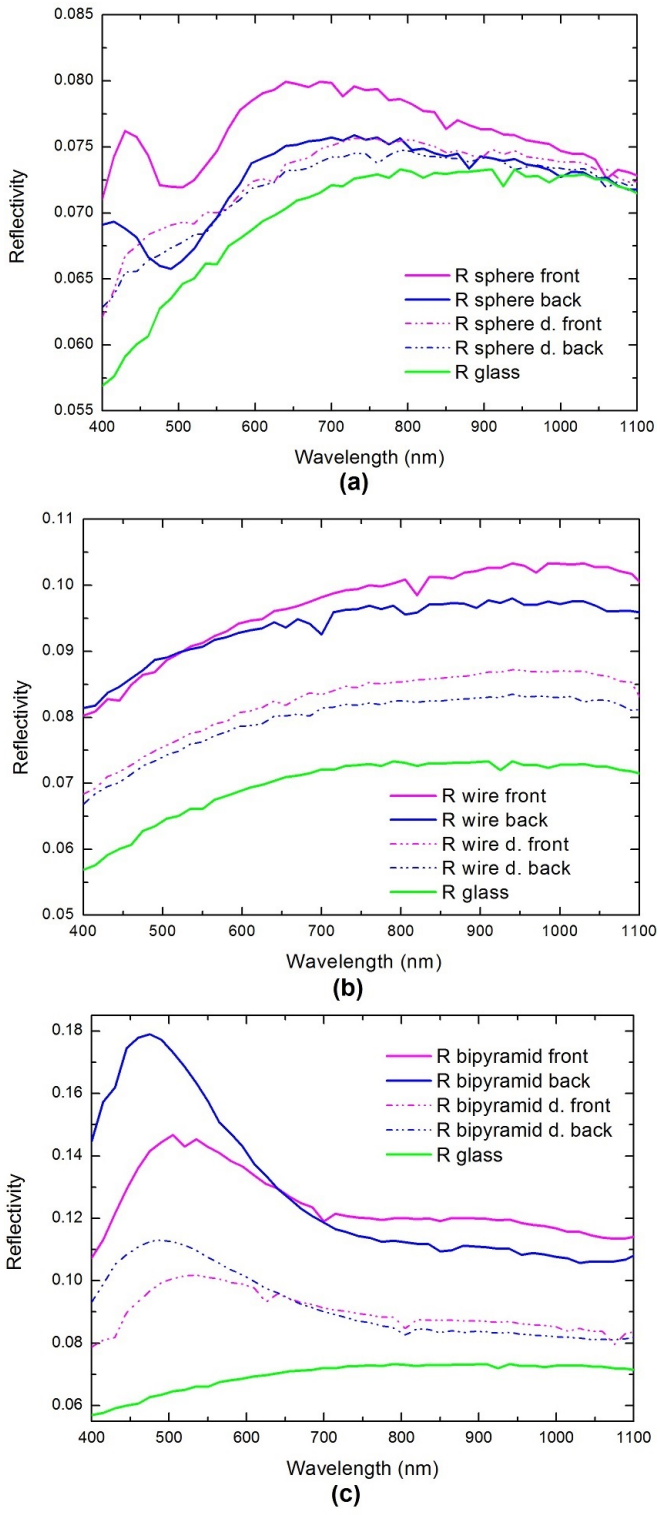

Figure 4.6: Total reflectivity measurements of (a) sphere and sphere d. samples (b) wire and wire d. samples (c) bipyramid and bipyramid d. samples.

nanowire samples respectively. Haze and diffuse transmission of the nanobipyramid sample reached up to 15 and 13 fold enhancement respectively at the peak position around 520 nm. The same spectral behaviors were observed in the total and diffuse reflectivity measurements, which are provided in Figure 4.9.

Last of all, extinction curves of the samples, were plotted and provided in Figure 4.10. It is clear that, extinction increased more in the UV region for all samples. Extinction curves did not show significant differences when the samples were illuminated from the glass and particle side except for the nanobipyramid sample.

4.2.2 Amorphous Silicon Deposited Sample Characterization

Optical measurements were affected from the deposition of a-Si:H. Reflectivity measurements of the a-Si:H deposited samples without a spacer layer, showed in Figure 4.11, indicated the thin film effect of the a-Si:H. Since the reflectivity measurement of the samples with spacer layer revealed the same characteristics, only a-Si:H deposited samples were plotted. It can be stated that, thin film interference effect at certain wavelengths were decreased with the reducing surface coverage of the samples. Although it is seen in all reflectivity measurements, this modulation can be seen clearly in bipyramids samples. The same characteristics in the total reflectivity of the Si_3N_4 deposited samples can be seen in Figure 4.12.

Scattering effect of MNPs at certain wavelengths can be interpreted from the dips appeared in the transmission measurements at wavelengths around 600 nm. The shape dependent shift in the dip between 550-650 nm wavelength interval can be seen in the diffuse transmission graph shown in the Figure 4.13. Figure 4.14 shows the red-shifted diffuse transmission curve of nanosphere sample in the presence of the spacer layer. This shift occured for all shapes and concentrations.

Shape dependency of extinction can be seen in Figure 4.15 in which differential extinction of nanopsphere, nanowire and nanobipyramid substrates with and without the spacer layer were plotted together. In both graphs, differential extinctions were calculated for the front side (particle side) of the samples by subtracting the extinction of reference sample from the extinction of the samples. Differential extinction curves

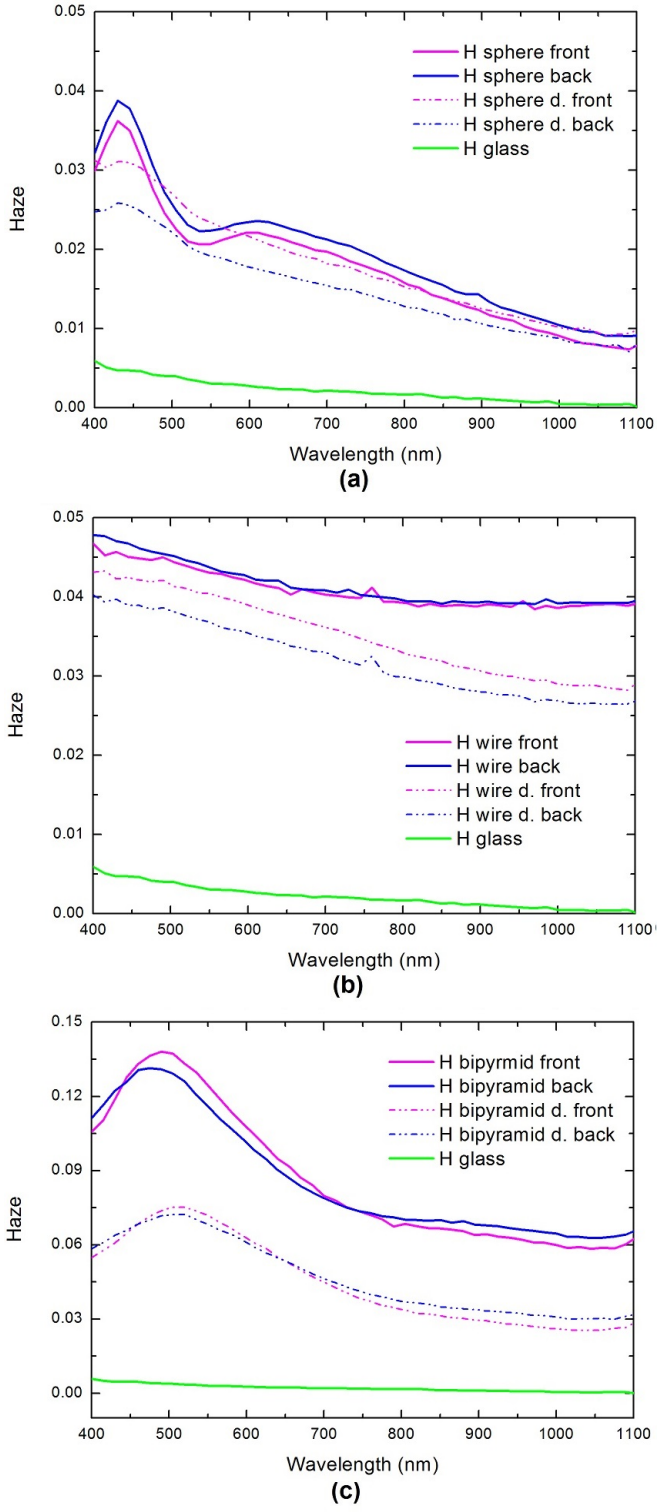

Figure 4.7: Haze of (a) sphere and sphere d. samples (b) wire and wire d. samples and (c) bipyramid and bipyramid d. samples.

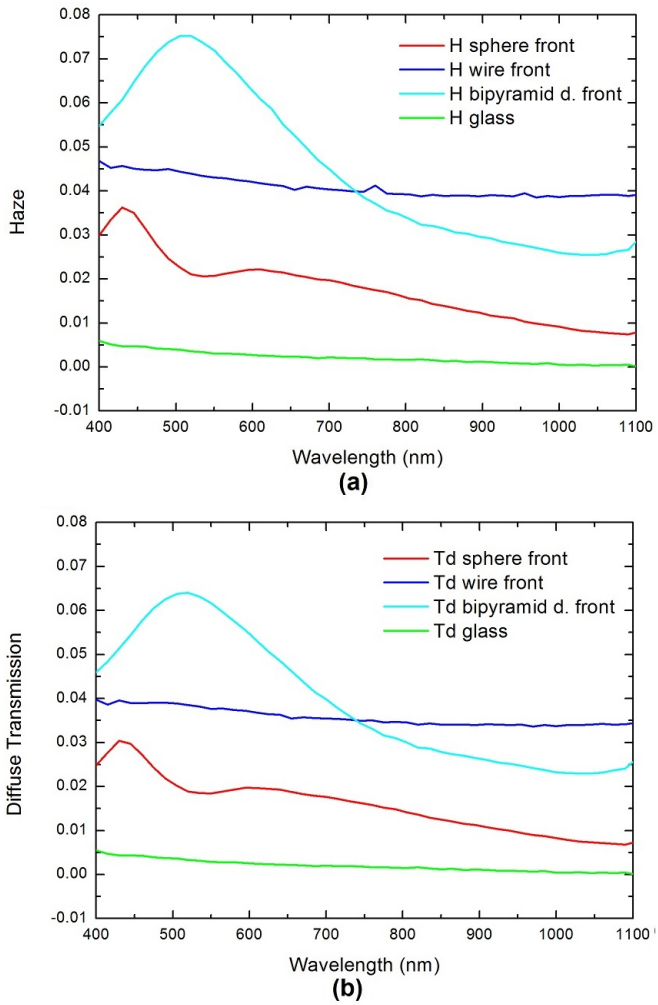

Figure 4.8: Shape dependency of (a) haze and (b) diffuse transmission.

had a peak around 600 nm for the samples deposited with a-Si:H and it red-shifted to about 650 nm for the samples deposited with passivation layer; Si_3N_4.

Consistent with the diffuse transmission data, haze graphs of the samples given in Figure 4.16 and Figure 4.17 resulted in dips around 600 nm. Larger values of haze were obtained for all samples when they were illuminated from the glass side (back side) of the particle. Haze of the bipyramid sample was enhanced by 30 times compared to the reference sample for both with and without the spacer layer. The purpose of the measurements to be done from both glass and a-Si:H deposited side was to see the preferential scattering of the light through the higher refractive index medium (it was a-Si:H medium in our case). This phenomenon was sketched and provided in

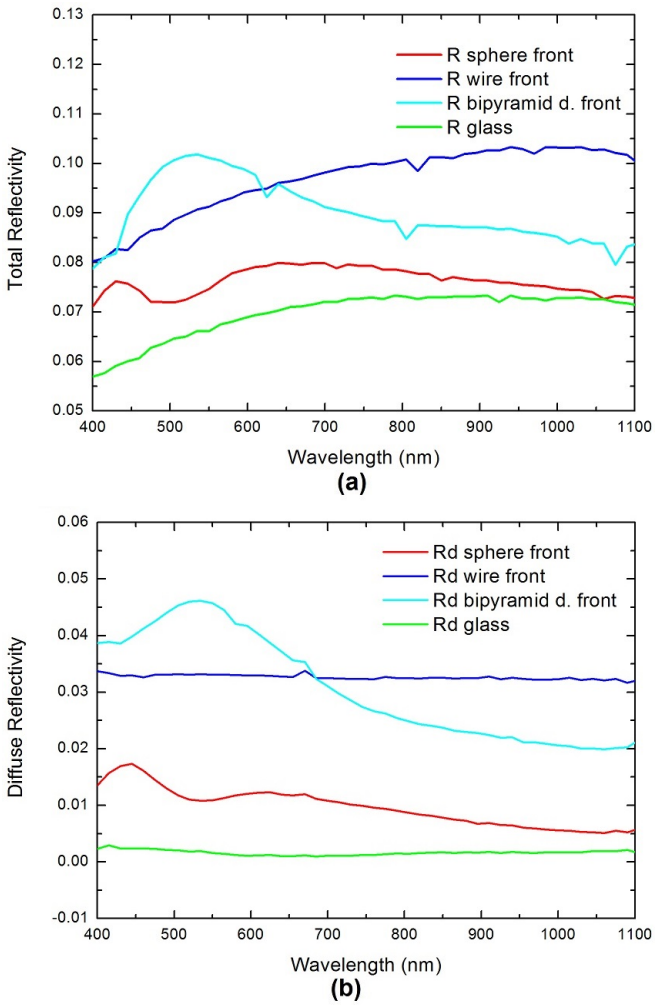

Figure 4.9: Shape dependency of (a) total and (b) diffuse reflectivity.

Figure 4.18.

Experimental results of the extinction was compared with the simulation of Mie theory [33]. Since Mie theory holds for spherical particles in the homogenous media, it is needed to define an effective dielectric constant for the surrounding media. For a sphere with a radius of 45 nm, lying on the glass and embedded in a-Si:H layer, effective dielectric constant was calculated by taking 40% of a-Si:H medium and 60% of the glass. For a nanosphere surrounded by a spacer layer of Si_3N_4 the percentages of the a-Si:H, glass and Si_3N_4 layers were calculated to be 30, 60 and 10 respectively, to calculate the effective dielectric constant. It was reported that, experimental results were consistent with the Mie theory simulation results, which can be seen in Figure

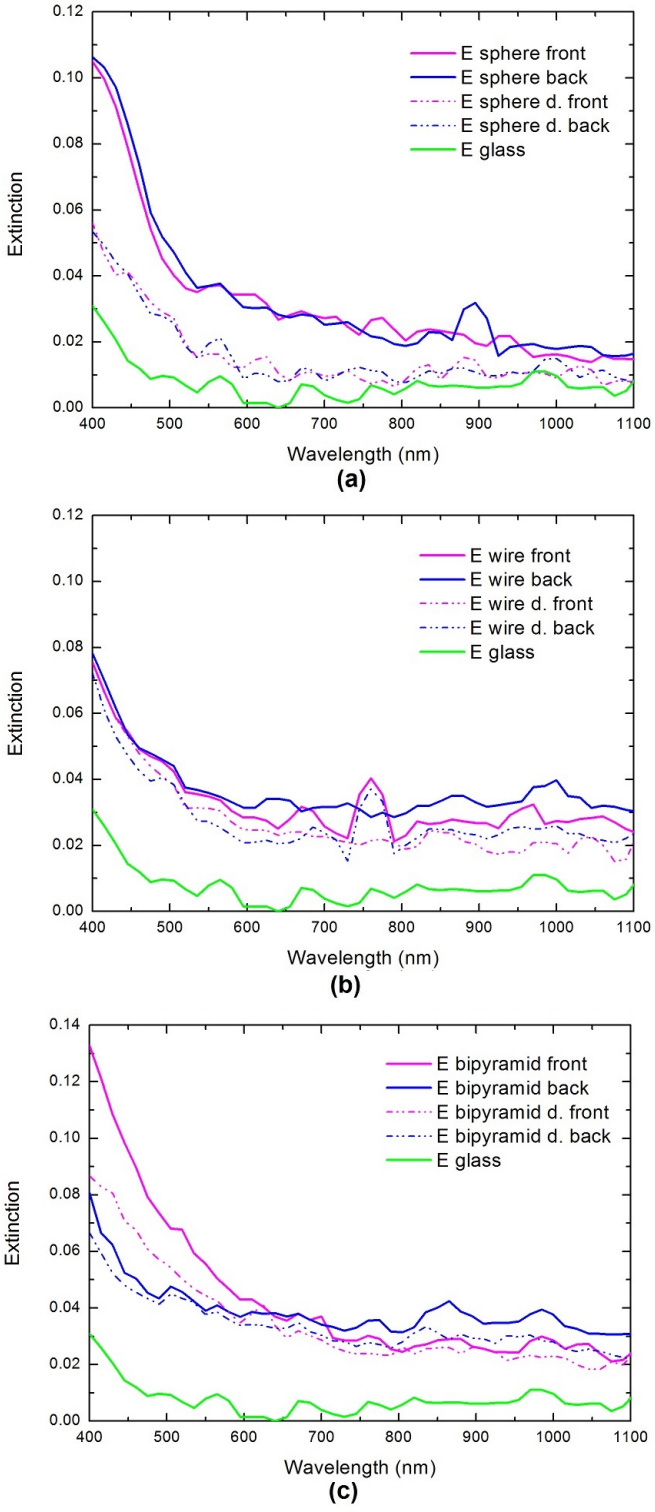

Figure 4.10: Extinction of (a) sphere and sphere d. samples (b) wire and wire d. samples (c) bipyramid and bipyramid d. samples.

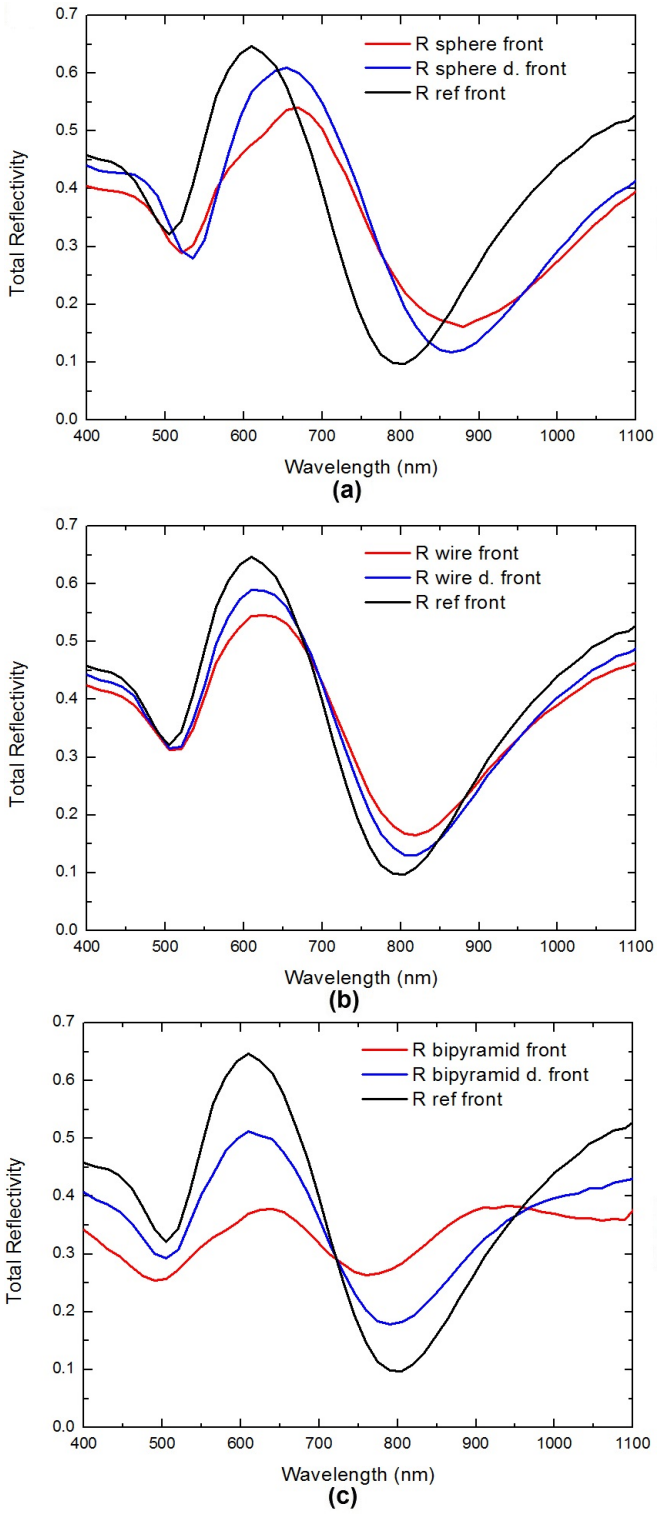

Figure 4.11: Total reflectivity of the (a) sphere samples, (b) wire samples and (c) bipyramid samples after the Si_3N_4 and a-Si:H deposition.

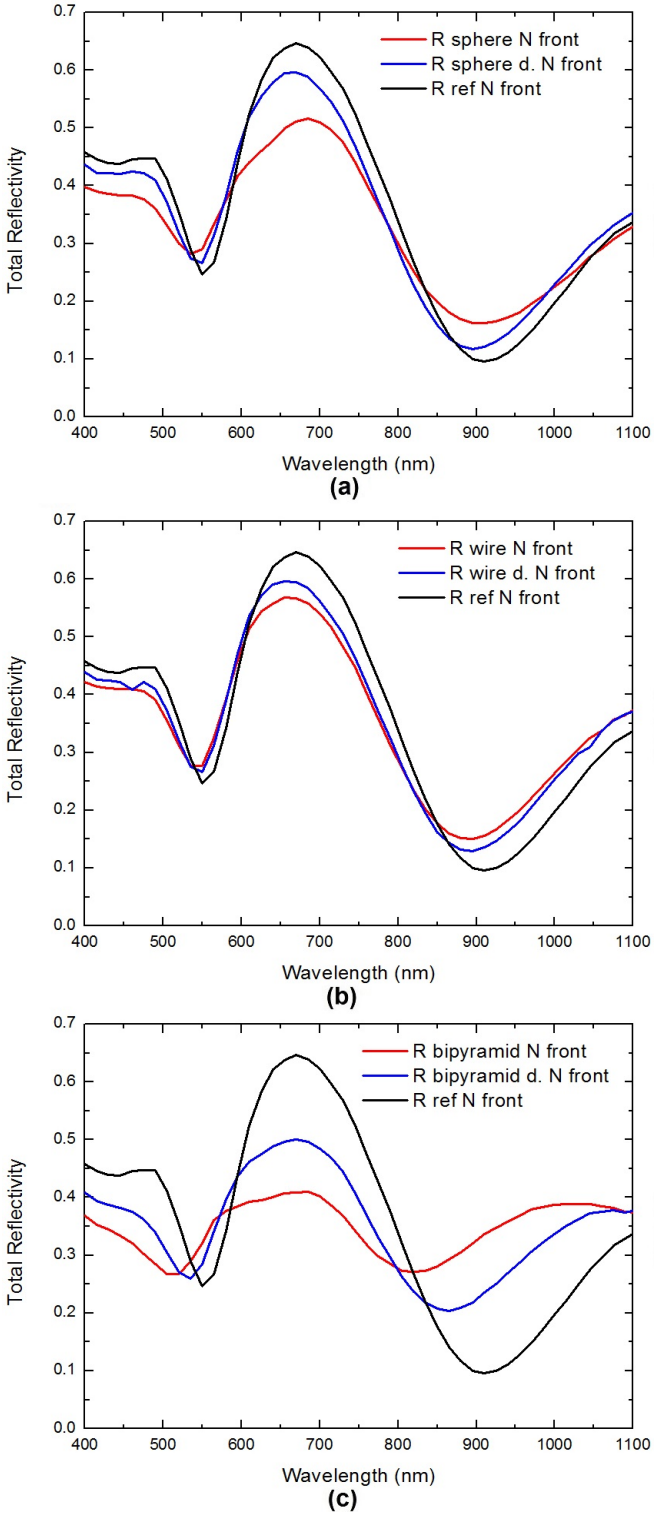

Figure 4.12: Total reflectivity of the (a) sphere samples, (b) wire samples and (c) bipyramid samples after the a-Si:H deposition

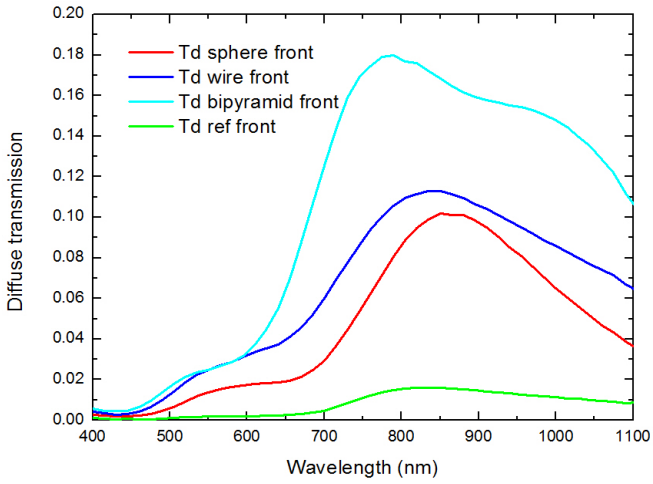

Figure 4.13: Diffuse transmission change for the a-Si:H deposited samples.

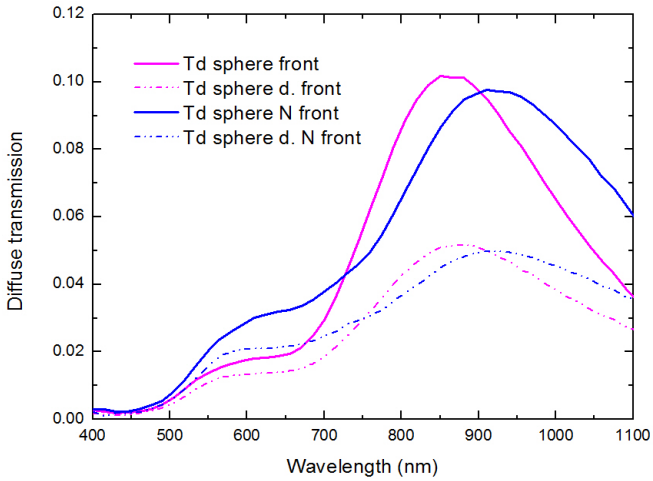

Figure 4.14: Diffuse transmission graph for nanosphere samples varying with the concentration and presence of spacer layer.

4.19 and Figure 4.20. Although simulation and experimental results were consistent with each other, the shift in the wavelength of the peak was observed since calculations by defining effective index did not give accurate results.

4.3 Spectral Photocurrent Results

In this section, spectral changes in the photoresponse measurement was correlated with the extinction curves of the a-Si:H deposited samples. Therefore, spectral pho-

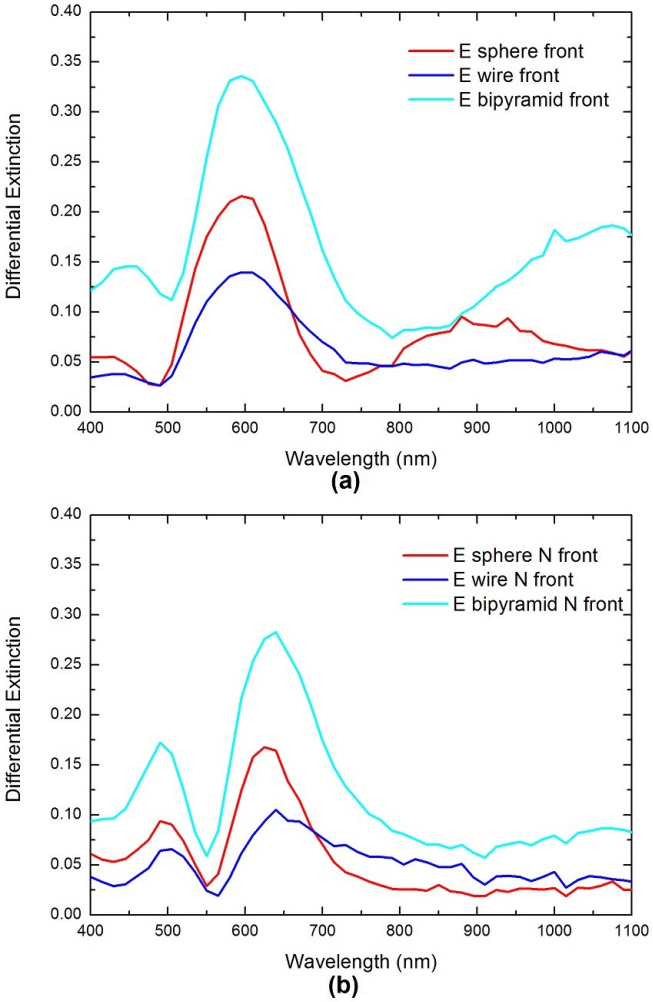

Figure 4.15: Shape dependency of differential extinction curve for (a) nanosphere, nanowire and nanobipyramid substrates (b) nanosphere N, nanowire N and nanobipyramid N substrates.

tocurrent graphs were plotted with extinction curves within the wavelength range of 400-1100 nm. Each photocurrent measurement was individually normalized and minimums of reference and samples were leveled to be able to trace the spectral behavior.

In Figure 4.21, extinction and normalized photoresponse graphs of substrates with nanospheres deposited with a-Si:H were given for both concentrations as sphere and sphere d. In Figure 4.22, extinction and normalized photoresponse graphs of substrates with nanowires deposited with a-Si:H were given for both concentrations as wire and wire d. In Figure 4.23, extinction and normalized photoresponse graphs of substrates with nanobipyramids deposited with a-Si:H were given for both concentra-

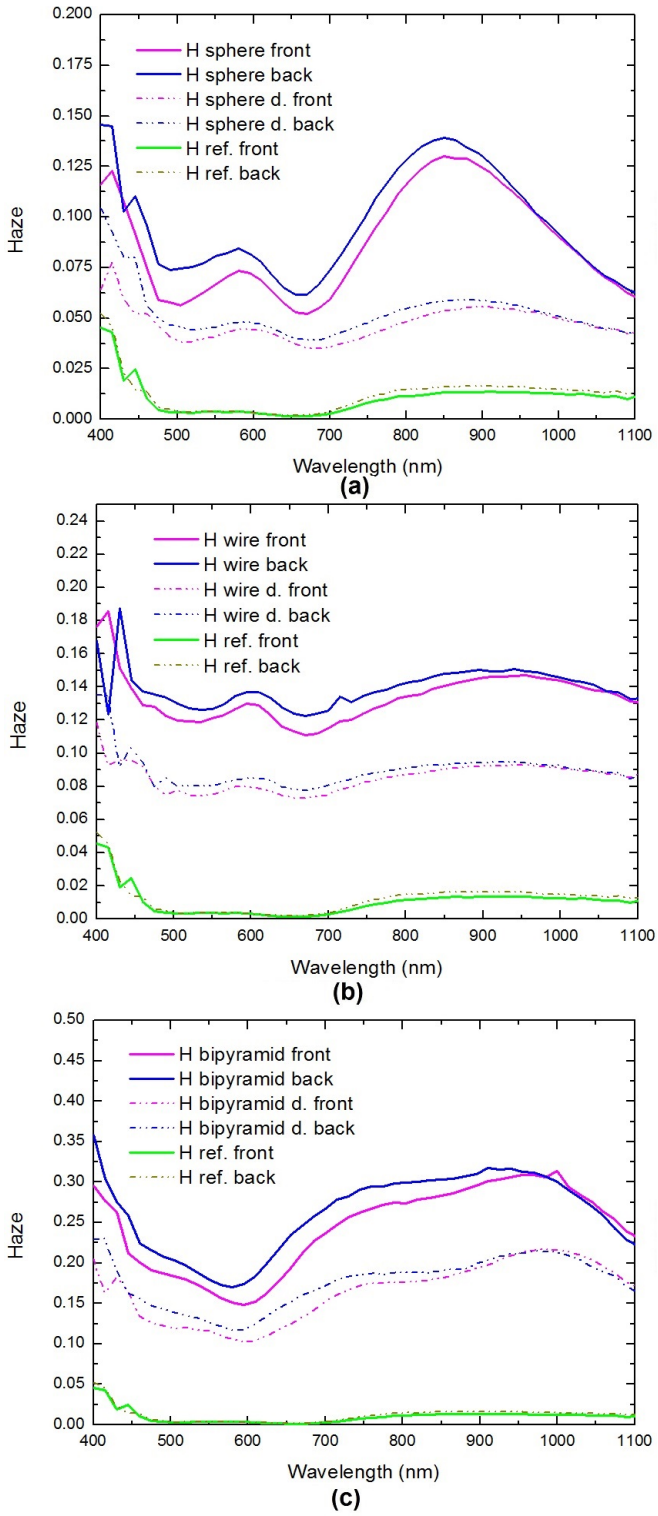

Figure 4.16: Haze graphs of a-Si:H deposited samples with the shapes (a) nanosphere (b) nanowire and (c) nanobipyramid.

tions as bipyramid and bipyramid d.

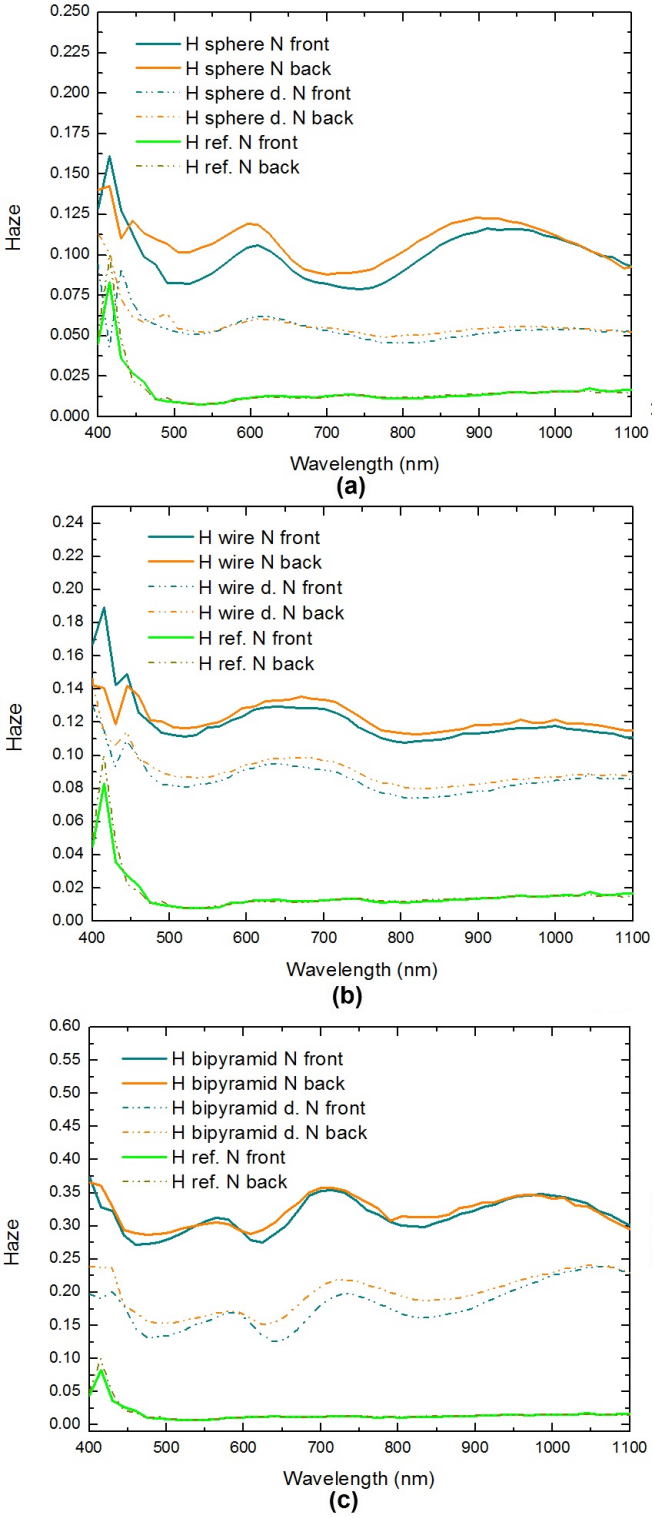

Figure 4.17: Haze graphs of a-Si:H and spacer layer deposited samples with the shapes (a) nanosphere (b) nanowire and (c) nanobipyramid.

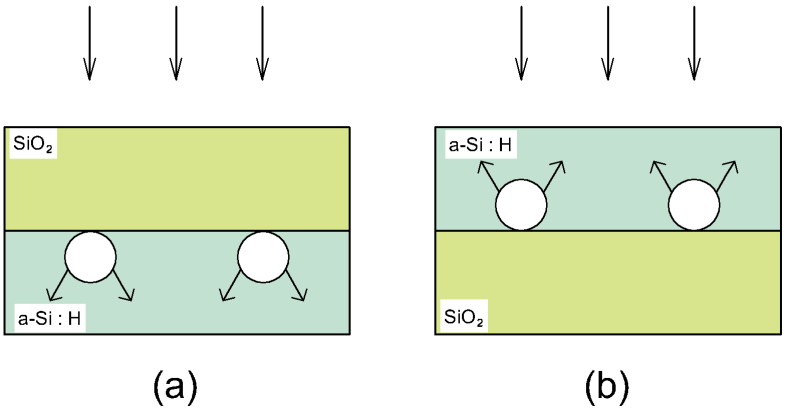

Figure 4.18: Preferential scattering of the light through the higher refractive index medium when illuminated from (a) glass side (b) a-Si:H side.

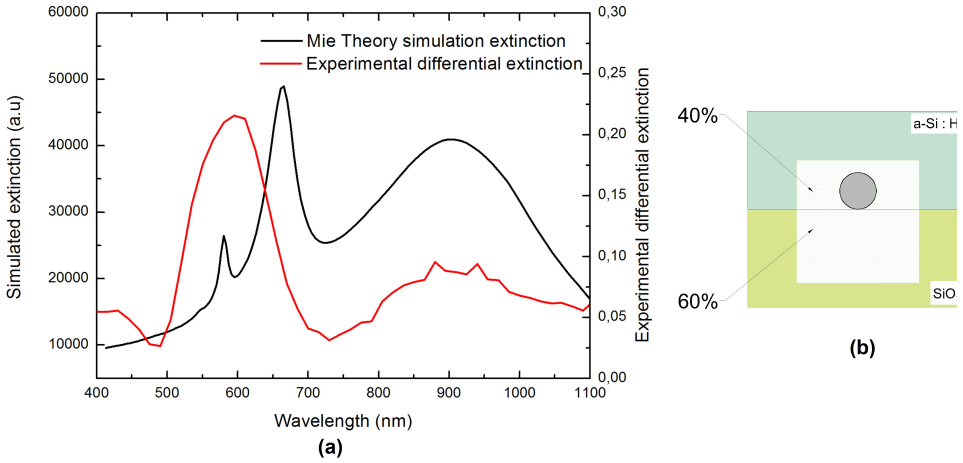

Figure 4.19: (a) Experimental differential extinction and Mie theory extinction simulation result for a nanosphere deposited with Si_3N_4 and a-Si:H (b) schematic view of calculation of effective dielectric constant.

In Figure 4.24, extinction and normalized photoresponse graphs of substrates with nanospheres deposited with a Si_3N_4 layer and a-Si:H were given for both concentrations as sphere N and sphere d. N. In Figure 4.25, extinction and normalized photoresponse graphs of substrates with nanowires deposited with a Si_3N_4 layer and a-Si:H were given for both concentrations as wire N and wire d. N. In Figure 4.26, extinction and normalized photoresponse graphs of substrates with nanobipyramids deposited with a Si_3N_4 layer and a-Si:H were given for both concentrations as bipyramid N and bipyramid d. N.

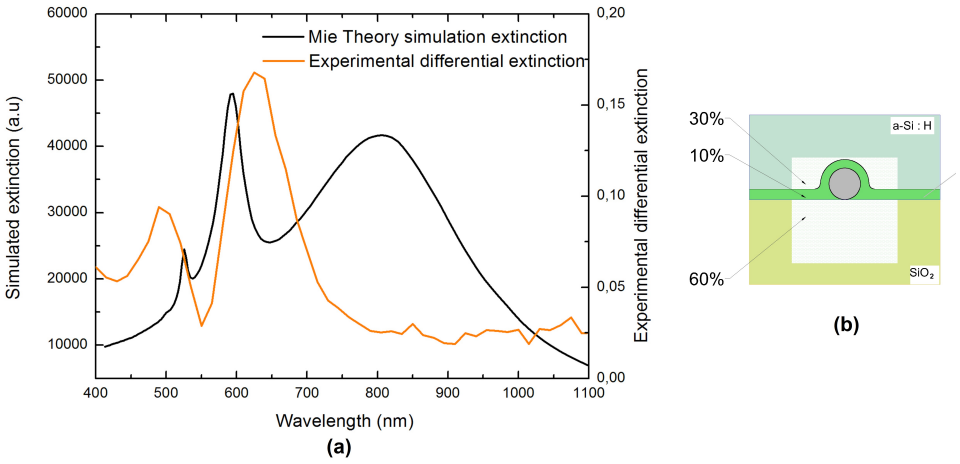

Figure 4.20: (a) Experimental differential extinction and Mie theory extinction simulation result for a nanosphere deposited with a-Si:H (b) schematic view of calculation of effective dielectric constant.

For all samples, the spectral photocurrent is red-shifted and broadened compared to the reference sample. It can be inferred from the correlation between extinction and phororesponse curves that broadening of the photoresponse curve can be attributed to the plasmonic effect. This plasmonic effect indicates that, there must be a scattering enhancement when there is plasmonic interfaces. The broadening appears within the wavelength range of 550-700 nm; although, it shifts with the change of sample.

Last of all, absolute values of the photoconductivity measurements obtained for the samples with a spacer layer were compared to the a-Si:H deposited glass substrate (reference) to see the effect of the MNPs. Photoresponse measurement in mA per incident power (W) versus wavelength can be seen in Figure 4.27. The photocurrent data of the reference sample was multiplied with 100 to be noticable in this range. The sample which enhanced the photocurrent mostly was found out to be nanowire. The sample decorated with the nanowire sample resulted in 600 fold enhancement compared to the reference. When the current-voltage characteristics of the samples with and without the spacer layer were compared, it was observed that, the surface passivation was achieved when there was a layer of Si_3N_4 between the MNPs and a-Si:H.

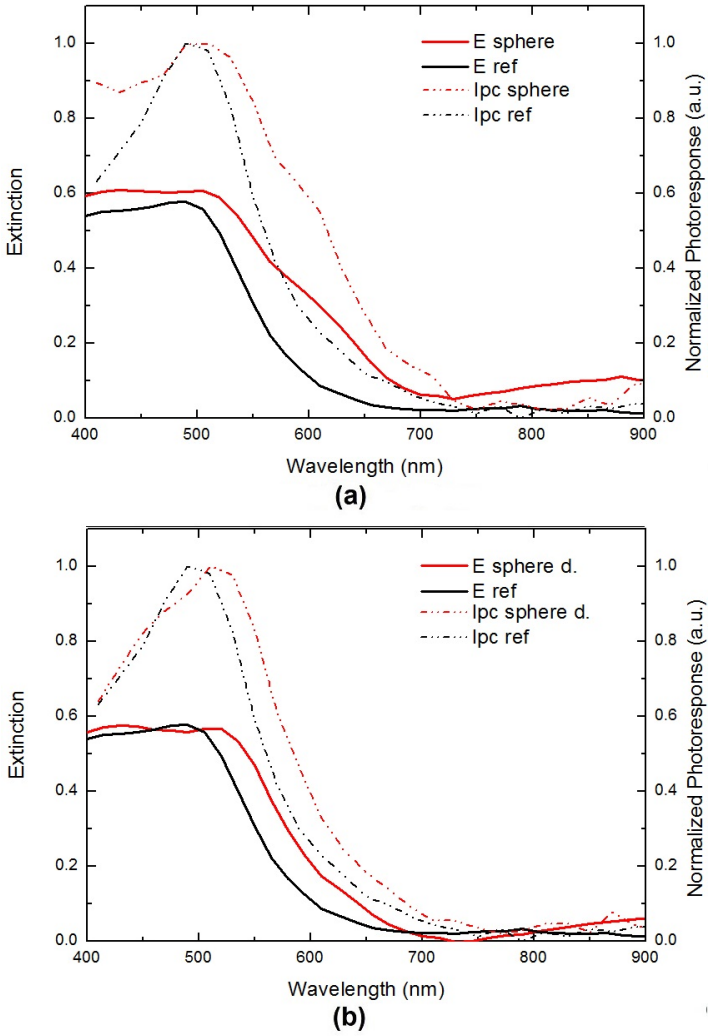

Figure 4.21: Extinction and normalized photoresponse graphs of nanosphere substrates with varying concentrations deposited with a-Si:H.

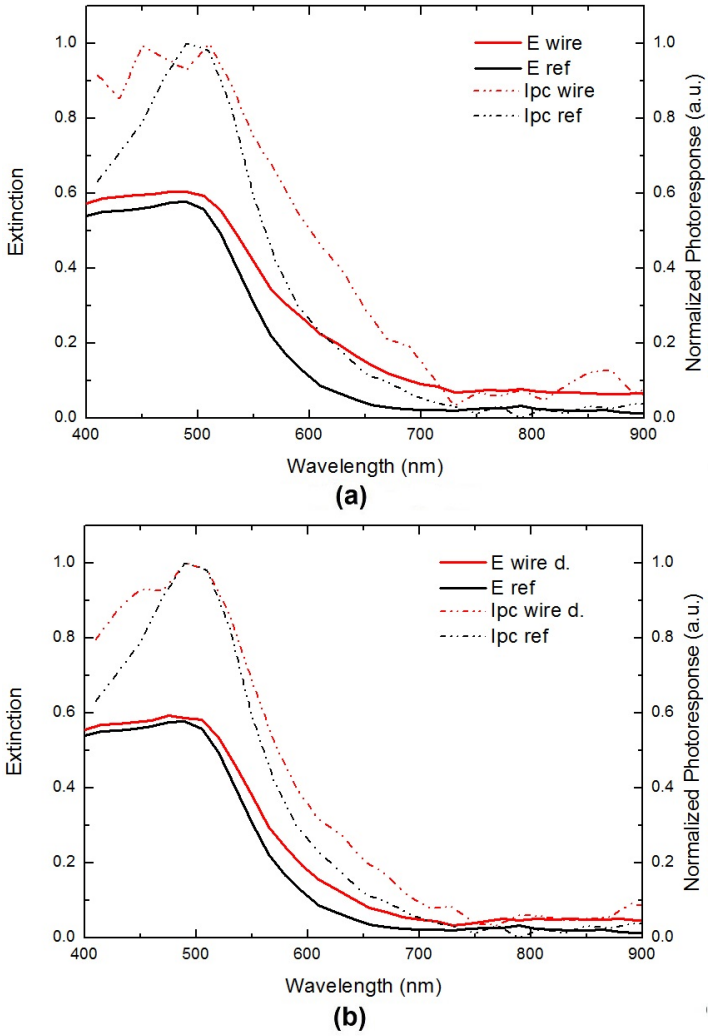

Figure 4.22: Extinction and normalized photoresponse graphs of nanowire substrates with varying concentrations deposited with a-Si:H.

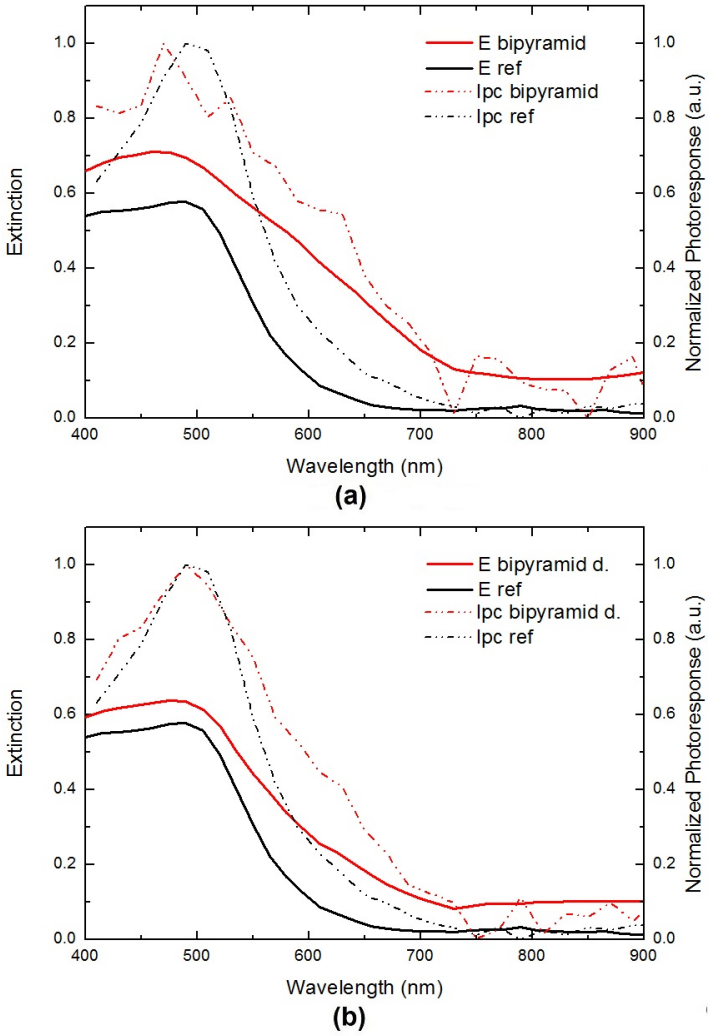

Figure 4.23: Extinction and normalized photoresponse graphs of nanobipyramid substrates with varying concentrations deposited with a-Si:H.

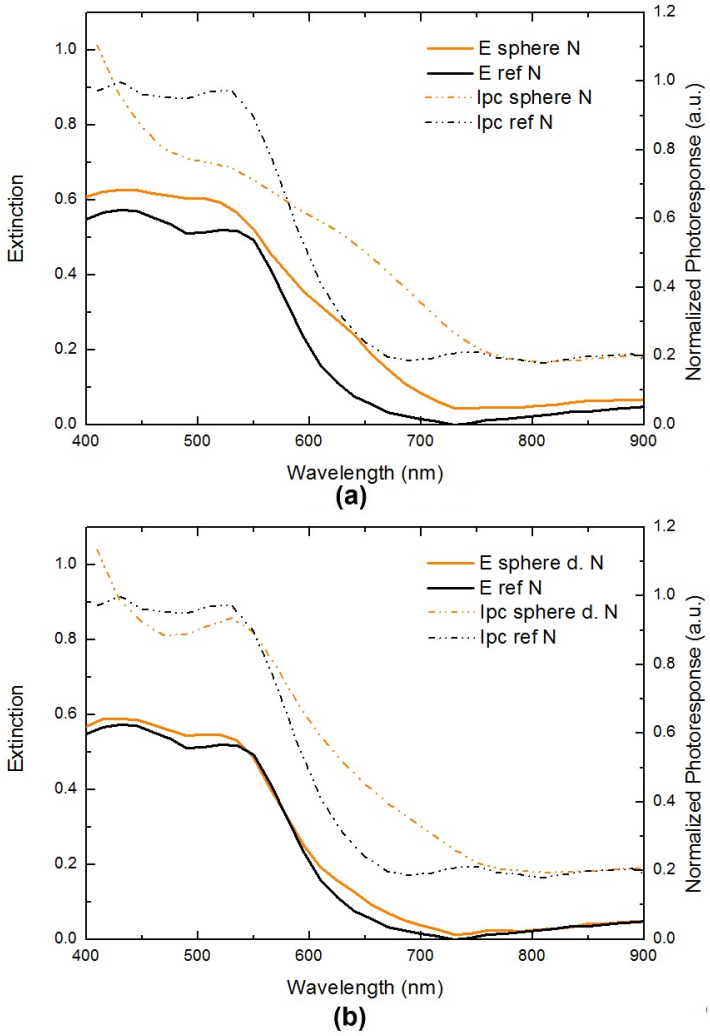

Figure 4.24: Extinction and normalized photoresponse graphs of nanosphere substrates with varying concentrations deposited with Si_3N_4 and a-Si:H.

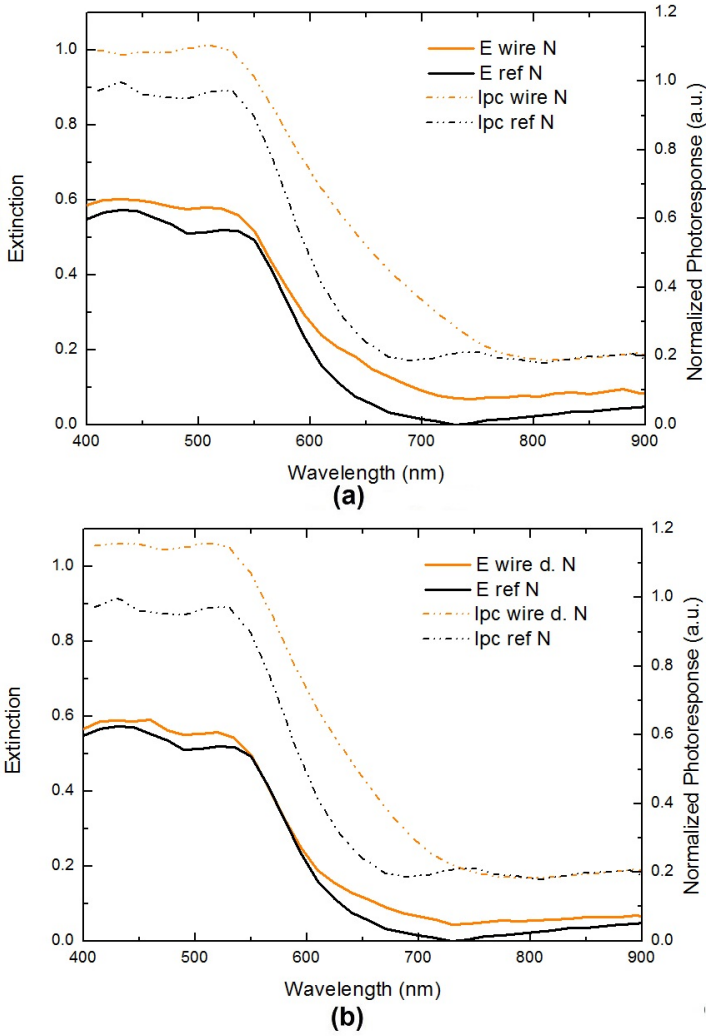

Figure 4.25: Extinction and normalized photoresponse graphs of nanowire substrates with varying concentrations deposited with Si_3N_4 and a-Si:H.

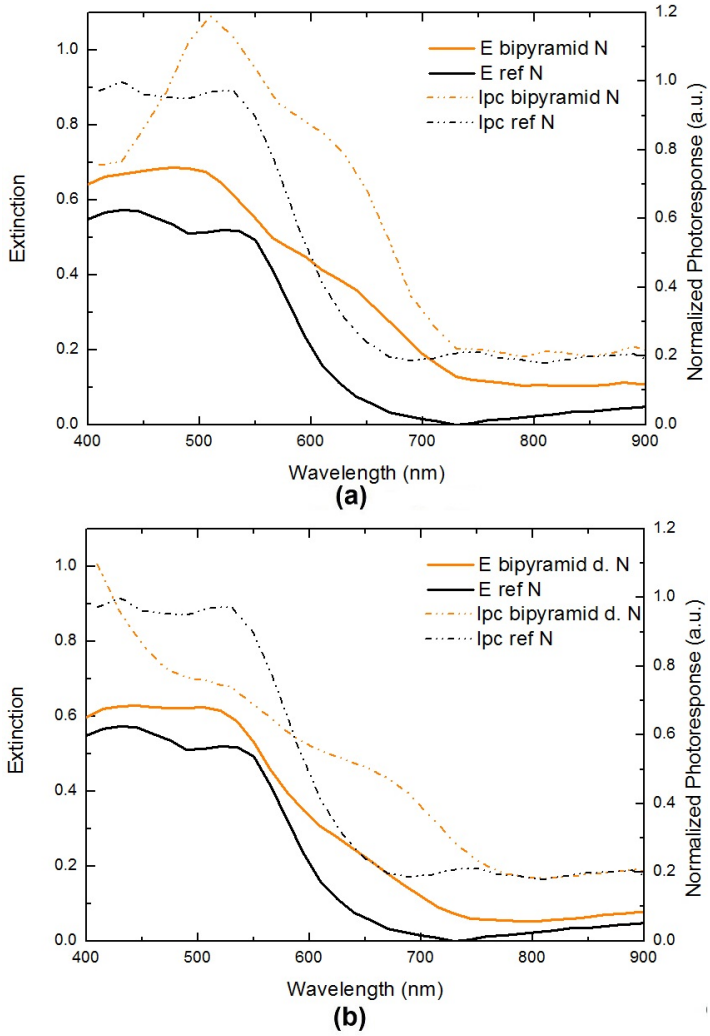

Figure 4.26: Extinction and normalized photoresponse graphs of nanobipyramid substrates with varying concentrations deposited with Si_3N_4 and a-Si:H.

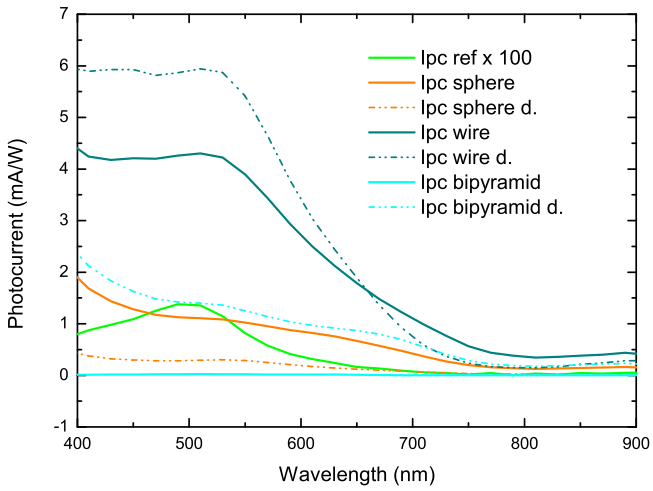

Figure 4.27: Absolute values of photocurrent measurements of samples with the spacer layer.

CHAPTER 5

CONCLUSION

In this thesis study, MNPs with different shapes were used to form plasmonic interfaces. Optical and electrical properties of the MNP decorated samples and a-Si:H deposited samples were investigated to figure out feasibility of plasmonics to solar cell applications. Ag was preferred as a material of the MNPs due to being less absorptive. However, oxidization problem of Ag NPs should be taken into account for the solar cell applications. The plasmonic properties of Ag nanospheres, nanowires and nanobipramids were investigated. These substrates were prepared with different concentrations to see the effect of the surface coverage of the MNPs on the optical and electrical properties. Besides the effect of the shape and concentration of the MNPs, the effect of the spacer layer was also investigated by using a layer. Optical characterization was carried out after the MNP decoration and a-Si:H deposition. In addition to reflectivity and transmission calculations, haze and extinction were measured to see the preferential scattering effect of the particles into the a-Si:H layer. Significant difference in the optical measurements was observed in the presence of MNPs; especially for the bipyramidal structures, which has sharp edges compared to the spheres and wires. Optical measurements showed that existence of MNPs enhanced the haze 3 to 15 times according to shape and concentration of the MNPs. After the a-Si:H deposition process, the haze of the sample decorated with nanobipyramid measured to be 30 times bigger than the haze of the sample without nanoparticle decoration.This increase indicates that use of MNPs in the junction of solar cells can lead to remarkable enhancement in the efficiency of solar cells. The plasmonic effect of nanospheres obtained in the experimental results were compared with the Mie theory using a widget to calculate extinction of a spherical particle in a homogenous medium and consistent

results were obtained. Both simulation and experimental results showed that plasmon resonance occured at the wavelength range of 600-700 nm for a nanosphere with a diameter about 90nm. After the optical characterization, the spectral photocurrent was measured from the same samples. The similar red-shifted broadening in both extinction and spectral photoresponse curves was observed. Therefore, normalized spectral photoresponse is correlated with the enhancement in the extinction in the same spectral range of 500-750 nm. Absolute values of photoresponse measurements compared with the reference sample without MNPs, resulted in an enhancement of the photoresponse up to a factor of 600, depending on the shape and concentration of the particles. This result reinforces the affirmative effect of MNPs in solar cell applications. This study showed that bipyramidal structures should be preferred to increase preferential scattering into the substrate.

To conclude, this study presented the feasibility of the use of different MNP shapes in the solar cell applications. Further investigation can be carried out on the uniformity and surface coverage of the MNPs on the substrates, passivation effect of the spacer layer with different materials and thicknesses. Experimental results can be verified using numerical or analytical methods which could give results with higher accuracy. Solar cells can be designed by using MNPs to increase the efficiency of the devices.

REFERENCES

[1] J. L. Sawin, "Renewables 2012 Global Status Report 2012," tech. rep., 2012.

[2] "Press Releases 2013," http://www.ise.fraunhofer.de/en/press-and-media/press-releases/presseinformationen-2013/world-record-solar-cell-with-44.7-efficiency last accesed on 21/08/2014.

[3] M. Faraday, "Experimental relations of gold (and other metals) to light," *Philosophical Transactions of the Royal Society of London*, vol. 147, pp. 145–181, Jan. 1857.

[4] J. C. M. Garnett, "Colours in metal glasses, in metallic films, and in metallic solutions. II," *Philosophical Transactions of the Royal Society A: Mathematical, Physical and Engineering Sciences*, vol. 205, pp. 237–288, Jan. 1906.

[5] I. Langmuir, "Oscillations in ionized gases," *Proceedings of the National Academy of Sciences*, vol. 14, pp. 627–637, Aug. 1928.

[6] D. Pines and D. Bohm, "Collective description of electron interactions:," *Physical Review*, vol. 85, no. 2, pp. 338–353, 1952.

[7] D. Pines, "Collective energy losses in solids," *Reviews of Modern Physics*, vol. 28, no. 3, pp. 184–198, 1956.

[8] E. Stern and R. Ferrell, "Surface Plasma Oscillations of a Degenerate Electron Gas," *Physical Review*, vol. 120, pp. 130–136, Oct. 1960.

[9] R. Ritchie, "Plasma Losses by Fast Electrons in Thin Films," *Physical Review*, vol. 106, 1957.

[10] A. Otto, "Excitation of nonradiative surface plasma waves in silver by the method of frustrated total reflection," *Zeitschrift für Physik*, vol. 216, pp. 398–410, 1968.

[11] E. Kretschmann and H. Reather, "Radiative decay of nonradiative surface plasmon excited by light," *Z. Naturforsch*, vol. A 23, pp. 2135–2136, 1968.

[12] H. R. Stuart and D. G. Hall, "Island size effects in nanoparticle-enhanced photodetectors," *Applied Physics Letters*, vol. 73, no. 26, pp. 3815–3817, 1998.

[13] D. M. Schaadt, B. Feng, and E. T. Yu, "Enhanced semiconductor optical absorption via surface plasmon excitation in metal nanoparticles," *Applied Physics Letters*, vol. 86, no. 6, p. 063106, 2005.

[14] S. Pillai, K. R. Catchpole, T. Trupke, and M. A. Green, "Surface plasmon enhanced silicon solar cells," *Journal of Applied Physics*, vol. 101, no. 9, p. 093105, 2007.

[15] D. Derkacs, S. H. Lim, P. Matheu, W. Mar, and E. T. Yu, "Improved performance of amorphous silicon solar cells via scattering from surface plasmon polaritons in nearby metallic nanoparticles," *Applied Physics Letters*, vol. 89, no. 9, p. 093103, 2006.

[16] A. Axelevitch, B. Gorenstein, and G. Golan, "Application of gold nano-particles for silicon solar cells efficiency increase," *Applied Surface Science*, pp. 10–13, 2014.

[17] A. J. Morfa, K. L. Rowlen, T. H. Reilly, M. J. Romero, and J. van de Lagemaat, "Plasmon-enhanced solar energy conversion in organic bulk heterojunction photovoltaics," *Applied Physics Letters*, vol. 92, no. 1, p. 013504, 2008.

[18] K. Nakayama, K. Tanabe and H. A. Atwater, "Plasmonic nanoparticle enhanced light absorption in GaAs solar cells," *Applied Physics Letters*, vol. 93, no. 12, p. 121904, 2008.

[19] M. Fleischmann, P. J. Hendra, and A. J. McQuillan, "Raman spectra of pyridine adsorbed at a silver electrode.," *Chemical Physics Letters*, vol. 26, pp. 163–166, 1974.

[20] Z. Zalevsky and I. Abdulhalim, *Integrated Nanophotonic Devices*. 2010.

[21] B. Liedberg, C. Nylander, and I. Lundstrom, "Surface plasmon resonance for gas detection and biosensing," *Sensors Actuators*, vol. 4, p. 299, 1983.

[22] U. Guler and R. Turan, "Effect of particle properties and light polarization on the plasmonic resonances in metallic nanoparticles.," *Optics express*, vol. 18, pp. 17322–38, Aug. 2010.

[23] I. Tanyeli, "Effect of substrate type on structural and optical properties of metal nanoparticles for plasmonic applications," 2011.

[24] Y. Yu and G. Zhang, *Updates in advanced lithography*. 2013.

[25] M. Zolfaghari Borra, "A feasibility study for external control on self-organized production of plasmonic enhancement interfaces for solar cells," 2013.

[26] P. Drude, "Zur Elektronentheorie der Metalle," *Annalen Der Physik*, vol. 306, no. 3, pp. 566–613, 1900.

[27] A. Trügler, *Optical properties of metallic nanoparticles*. PhD thesis, 2011.

[28] S. Lee, B. Kim, H. Kim, and Y. Lim, "The use of plasmonics in light beaming and focusing," *Progress in Quantum Electronics*, vol. 34, pp. 47–87, Mar. 2010.

[29] M. I. Mishchenko, L. D. Travis, and A. A. Lacis, *Scattering, absorption and emission of light by small particles*. Cambridge University Press, 2002.

[30] H. C. van de Hulst, *Light Scattering by Small Particles*. Courier Dover Publications, 1981.

[31] G. Mie, "Beiträge zur Optik trüber Medien speziell kolloidaler Metallö sungen," *Annalen Der Physik*, 1908.

[32] P. Debye, "Der lichtdruck auf kugeln von beliebigem material," *Annalen der Physik*, vol. 335, no. 11, pp. 57–136, 1909.

[33] "Mie light scattering by a single sphere," http://garciadeabajos-group.icfo.es/ last accesed on 20/08/2014.

[34] K. R. Catchpole and A. Polman, "Plasmonic solar cells," *Optics express*, vol. 16, pp. 21793–800, Dec. 2008.

[35] W. S. O. K. Akimov, Y. A. Koh, "Enhancement of optical absorption in thin-film solar cells through the excitation of higher-order nanoparticle plasmon modes," *Optics express*, vol. 17, pp. 10195–205, June 2009.

[36] S. A. Maier and H. A. Atwater, "Plasmonics: Localization and guiding of electromagnetic energy in metal/dielectric structures," *Journal of Applied Physics*, vol. 98, no. 1, p. 011101, 2005.

[37] K. R. Catchpole and A. Polman, "Design principles for particle plasmon enhanced solar cells," *Applied Physics Letters*, vol. 191113, no. 2008, pp. 1–4, 2012.

[38] H. A. Atwater and A. Polman, "Plasmonics for improved photovoltaic devices.," *Nature materials*, vol. 9, pp. 205–13, Mar. 2010.

[39] S. Coskun, B. Aksoy, and H. E. Unalan, "Polyol ynthesis of silver nanowires : an extensive parametric study," *Crystal Growth Design*, vol. 11, pp. 4963–4969, 2011.

[40] B. J. Wiley, Y. Xiong, Z. Li, Y. Yin, and Y. Xia, "Right bipyramids of silver: a new shape derived from single twinned seeds.," *Nano letters*, vol. 6, pp. 765–8, Apr. 2006.

APPENDIX A

MIE THEORY

To solve the problem we start from the scalar wave function which satisfy Maxwell's equations

$$\nabla^2\psi + k^2m^2\psi = 0 \tag{A.1}$$

It is a separable function in spherical polar coordinates so the solution will be in the form of Associated Legendre polynomials and spherical Bessel function.

$$\psi_{\ell n} = \left.\begin{matrix}\cos\ell\varphi \\ \sin\ell\varphi\end{matrix}\right\} P_n^{\ell}(\cos\theta) z_n(mkr) \tag{A.2}$$

and $z_n(\rho)$ is given in terms of Bessel function Z

$$z_n(\rho) = \sqrt{\frac{\pi}{2\rho}} Z_{n+1/2}(\rho) \tag{A.3}$$

The general solution of the scalar wave function becomes linear combinations of these functions given above. We can implement from the solution of the scalar wave equation that vector wave equation $\nabla^2\vec{A} + k^2m^2\vec{A} = 0$ is satisfied by the derived vector fields which are defined below.

$$\vec{M}_\psi = \vec{\nabla} \times (r\vec{\psi}) \tag{A.4}$$

$$mk\vec{N}_\psi = \vec{\nabla} \times \vec{M}_\psi \tag{A.5}$$

$$mk\vec{M}_\psi = \vec{\nabla} \times \vec{N}_\psi \tag{A.6}$$

Since u and v are the two solutions of the scalar wave equation, field vectors satisfied by the Maxwell's equations can be written in terms of these derived vectors fields; M_u, N_u, M_v, N_v.

$$\vec{E} = \vec{M}_v + i\vec{N}_u \tag{A.7}$$

$$\vec{H} = m(-\vec{M}_v + i\vec{N}_v) \tag{A.8}$$

If we assume the incident wave to be linearly polarized with an amplitude 1, propagation direction of the incident wave to be z−direction, and outside medium to be vacuum; $m_2 = 1$ incident wave can be described by the following equations.

$$\vec{E} = e^{-ikz+i\omega t}\hat{i} \tag{A.9}$$

$$\vec{H} = e^{-ikz+i\omega t}\hat{j} \tag{A.10}$$

İncident and scattered wave can also be chosen in the form of solutions of scalar wave equation for the elementary solution for $\ell = 1$ in the outer medium. Outside, incident wave:

$$u = e^{i\omega t}\cos\varphi \sum_{n=1}^{\infty} (-i)^n \frac{2n+1}{n(n+1)} P_n^1(\cos\theta) j_n(kr)$$

$$v = e^{i\omega t}\sin\varphi \sum_{n=1}^{\infty} (-i)^n \frac{2n+1}{n(n+1)} P_n^1(\cos\theta) j_n(kr) \tag{A.11}$$

j_n is Spherical Bessel function and it can be derived by using first kind Bessel function; $J_{n+1/2}$. Outside, scattered wave:

$$u = e^{i\omega t}\cos\varphi \sum_{n=1}^{\infty} -a_n(-i)^n \frac{2n+1}{n(n+1)} P_n^1(\cos\theta) h_n^{(2)}(kr)$$

$$v = e^{i\omega t}\sin\varphi \sum_{n=1}^{\infty} -b_n(-i)^n \frac{2n+1}{n(n+1)} P_n^1(\cos\theta) h_n^{(2)}(kr) \tag{A.12}$$

Inside wave:

$$u = e^{i\omega t}\cos\varphi \sum_{n=1}^{\infty} mc_n(-i)^n \frac{2n+1}{n(n+1)} P_n^1(\cos\theta) j_n(mkr)$$

$$v = e^{i\omega t}\sin\varphi \sum_{n=1}^{\infty} md_n(-i)^n \frac{2n+1}{n(n+1)} P_n^1(\cos\theta) j_n(mkr) \tag{A.13}$$

These solutions end up with four coefficients; a_n, b_n, c_n, d_n to be determined by applying boundary conditions. The terms of field components satisfying the boundary conditions are v and $\frac{1}{m}\frac{\partial(ru)}{\partial r}$ for E_θ and E_φ; mu and $\frac{\partial(rv)}{\partial r}$ for H_θ and H_φ respectively for $r = a$ where a is the radius of the sphere. Continuity of the given terms results in

equations in terms of Ricatti Bessel functions.

$$\begin{aligned}
[mu] \quad &: \quad \psi_n(x) - a_n\xi_n(x) = mc_n\psi_n(y) \\
\left[\frac{1}{m}\frac{\partial(ru)}{\partial r}\right] \quad &: \quad \psi_n'(x) - a_n\xi_n'(x) = c_n\psi_n'(y) \\
[v] \quad &: \quad \psi_n(x) - b_n\xi_n(x) = d_n\psi_n(y) \\
\left[\frac{\partial(rv)}{\partial r}\right] \quad &: \quad \psi_n'(x) - b_n\xi_n'(x) = md_n\psi_n'(y)
\end{aligned} \tag{A.14}$$

where Ricatti Bessel fuctions are defined below.

$$\begin{aligned}
\psi_n(z) &= zj_n(z) = (\pi z/2)^{1/2}J_{n+1/2}(z) \\
\xi_n(z) &= zh_n^{(2)}(z) = (\pi z/2)^{1/2}H_{n+1/2}^{(2)}(z)
\end{aligned} \tag{A.15}$$

$x = ka = \frac{2\pi a}{\lambda}$ and $y = mka$

The coefficients are found to be as follows.

$$\begin{aligned}
a_n &= \frac{\psi_n'(y)\psi_n(x) - m\psi_n(y)\psi_n'(x)}{\psi_n'(y)\xi_n(x) - m\psi_n(y)\xi_n'(x)} \\
b_n &= \frac{m\psi_n'(y)\psi_n(x) - \psi_n(y)\psi_n'(x)}{m\psi_n'(y)\xi_n(x) - \psi_n(y)\xi_n'(x)} \\
c_n &= \frac{\psi_n'(x)\xi_n(x) - \psi_n(x)\xi_n'(x)}{\psi_n'(y)\xi_n(x) - m\psi_n(y)\xi_n'(x)} \\
d_n &= \frac{\psi_n'(x)\xi_n(x) - \psi_n(x)\xi_n'(x)}{m\psi_n'(y)\xi_n(x) - \psi_n(y)\xi_n'(x)}
\end{aligned} \tag{A.16}$$

Scattered wave can be written as the following equations due to the asymptotic behavior of the spherical Bessel function.

$$\begin{aligned}
u &= -\frac{i}{kr}e^{-ikr+i\omega t}\cos\varphi\sum_{n=1}^{\infty}a_n\frac{2n+1}{n(n+1)}P_n^1(\cos\theta) \\
v &= -\frac{i}{kr}e^{-ikr+i\omega t}\sin\varphi\sum_{n=1}^{\infty}b_n\frac{2n+1}{n(n+1)}P_n^1(\cos\theta)
\end{aligned} \tag{A.17}$$

Scattered field components can be written in terms of amplitude functions which show the character of the fields.

$$E_\theta = H_\varphi = -\frac{i}{kr}e^{-ikr+i\omega t}\cos\varphi S_2(\theta)$$

$$-E_\varphi = H_\theta = -\frac{i}{kr} e^{-ikr+i\omega t} \sin\varphi S_1(\theta) \tag{A.18}$$

where

$$S_1(\theta) = \sum_{n=1}^{\infty} \frac{2n+1}{n(n+1)} \{a_n \pi_n(\cos\theta) + b_n \tau_n(\cos\theta)\}$$

$$S_2(\theta) = \sum_{n=1}^{\infty} \frac{2n+1}{n(n+1)} \{b_n \pi_n(\cos\theta) + a_n \tau_n(\cos\theta)\} \tag{A.19}$$

Two functions of Legendre polynomials used for simplification in amplitude functions are defined as follows.

$$\pi_n(\cos\theta) = \frac{1}{\sin\theta} P_n^1(\cos\theta)$$

$$\tau_n(\cos\theta) = \frac{d}{d\theta} P_n^1(\cos\theta)$$